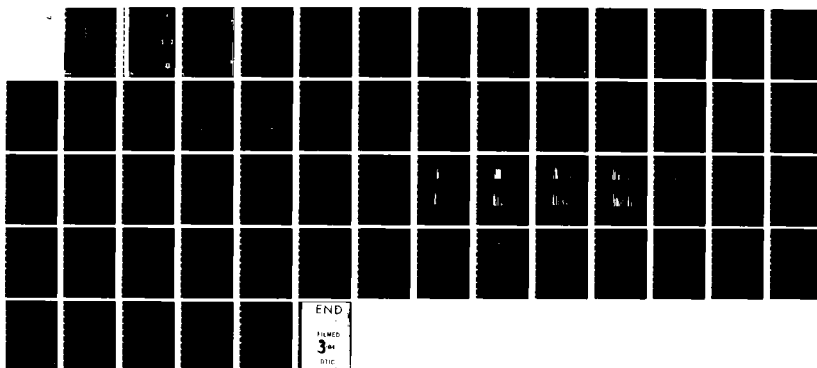
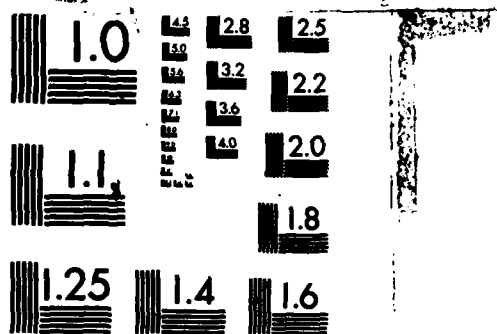


AD-A137 916 COCHISE OBSERVATIONS OF ANGON RYDBERG EMISSION FROM 2
TO 16 MICROMETERS(U) AIR FORCE GEOPHYSICS LAB HANSCOM
AFB MA W T RAWLINS ET AL. 05 AUG 83 AFGL-TR-83-0201
F/G 20/6 NL

UNCLASSIFIED



END
FILED
3-1
DTIC



MICROCOPY RESOLUTION TEST CHART
NATIONAL BUREAU OF STANDARDS-1963-A

ADA137916

AFGL-TR-83-0201
ENVIRONMENTAL RESEARCH PAPERS, NO. 840



12

COCHISE Observations of Argon Rydberg Emission From 2 to 16 Micrometers

W. T. RAWLINS
A. GELB
R. A. ARMSTRONG

5 August 1983

DTIC
ELECTED
S FEB 15 1984 D
A
B

Approved for public release; distribution unlimited.

OPTICAL PHYSICS DIVISION
AIR FORCE GEOPHYSICS LABORATORY
HANSCOM AFB, MASSACHUSETTS 01731

PROJECT 2310

AIR FORCE SYSTEMS COMMAND, USAF



84 02 15 027

DTIC FILE COPY

This report has been reviewed by the ESD Public Affairs Office (PA) and is releasable to the National Technical Information Service (NTIS).

*This technical report has been reviewed and is approved for publication"

FOR THE COMMANDER


(Signature)
RANDALL E. MURPHY
Branch Chief


(Signature)
JOHN S. GARING
Division Director

Qualified requestors may obtain additional copies from the Defense Technical Information Center. All others should apply to the National Technical Information Service.

If your address has changed, or if you wish to be removed from the mailing list, or if the addressee is no longer employed by your organization, please notify AFGL/DAA, Hanscom AFB, MA 01731. This will assist us in maintaining a current mailing list.

Do not return copies of this report unless contractual obligations or notices on a specific document requires that it be returned.

Unclassified

SECURITY CLASSIFICATION OF THIS PAGE (When Data Entered)

DD FORM 1 JAN 70 1473 EDITION OF 1 NOV 65 IS OBSOLETE

Unclassified

~~SECURITY CLASSIFICATION OF THIS PAGE (When Data Entered)~~

Unclassified

SECURITY CLASSIFICATION OF THIS PAGE(When Data Entered)

20. Abstract (Contd)

cont

ionization limit. These states must have kinetically enhanced populations in order to account for the observed emission intensities. The results are interpreted in terms of a radiative/collisional cascade sequence initiated by dissociative recombination of Ar²⁺ with energetic electrons in the active discharge. The implications of these observations for atmospheric infrared signatures are discussed.



Ar 2 (4)

Unclassified

SECURITY CLASSIFICATION OF THIS PAGE(When Data Entered)

Contents

1. INTRODUCTION	7
2. EXPERIMENTAL OBSERVATIONS	9
3. INFRARED SPECTROSCOPY OF ArI	18
3.1 Argon Rydberg States	18
3.2 Calculation of Radiative Transition Probabilities	19
4. RESULTS OF SPECTRAL ANALYSIS	24
5. DISCUSSION	45
5.1 Kinetic Interpretations	45
5.2 Upper Atmospheric Implications	52
6. CONCLUSIONS	53
REFERENCES	55
DISTRIBUTION LIST	57

Illustrations

1. COCHISE Reaction Chamber	10
2. Survey of Ar SWIR Emission, 0.04-μm Resolution, 1 Torr	12
3. Survey of Ar MWIR Emission, 0.04-μm Resolution, 0.1 Torr	12
4. Survey of Ar LWIR Emission, 0.08-μm Resolution, 0.1 Torr	13

Illustrations

5. ArI Intensity at 12.2 μm as a Function of Total Ar Pressure in Discharge Sidearms	13
6. ArI Intensity at 12.2 μm as a Function of O ₂ Level in the Discharge Tubes, P _{Ar} = 1.3 Torr	14
7. High Resolution Spectrum of Ar Emission From 2 to 4 μm , 0.007- μm Resolution, 0.1 Torr	14
8. Medium Resolution Spectrum of Ar Emission, 4 to 5 μm , 0.013- μm Resolution, 0.1 Torr	15
9. High Resolution Spectrum of Ar Emission Near 4 μm , 0.007- μm Resolution, 0.1 Torr	15
10. Medium Resolution Spectrum of Ar Emission, 10 to 12 μm , 0.027- μm Resolution, 0.1 Torr	16
11. Medium Resolution Spectrum of Ar Emission, 12 to 15 μm , 0.027- μm Resolution, 0.1 Torr	16
12. High Resolution Spectrum of Ar Emission Near 12.3 μm , 0.013- μm Resolution, 0.1 Torr	17
13. Energy Level Diagram for Rydberg States of Argon	20
14. Computed Values of gA as a Function of Transition Wave- length (2 to 16 μm) for Argon Excited States, [1s ² 2s ² 2p ⁶ 3s ² 3p ⁵] n1, n=4	33
15. Computed Values of gA as a Function of Transition Wave- length (2 to 16 μm) for Argon Excited States, [1s ² 2s ² 2p ⁶ 3s ² 3p ⁵] n1, n=5	33
16. Computed Values of gA as a Function of Transition Wave- length (2 to 16 μm) for Argon Excited States, [1s ² 2s ² 2p ⁶ 3s ² 3p ⁵] n1, n=6	34
17. Computed Values of gA as a Function of Transition Wave- length (2 to 16 μm) for Argon Excited States, [1s ² 2s ² 2p ⁶ 3s ² 3p ⁵] n1, n=7	34
18. Computed Values of gA as a Function of Transition Wave- length (2 to 16 μm) for Argon Excited States, [1s ² 2s ² 2p ⁶ 3s ² 3p ⁵] n1, n=8	35
19. Computed Values of gA as a Function of Transition Wave- length (2 to 16 μm) for Argon Excited States, [1s ² 2s ² 2p ⁶ 3s ² 3p ⁵] n1, n=10	35
20. Computed Values of gA as a Function of Transition Wave- length (2 to 16 μm) for Argon Excited States, [1s ² 2s ² 2p ⁶ 3s ² 3p ⁵] n1, n=12	36
21. Computed Values of gA as a Function of Transition Wave- length (2 to 16 μm) for Argon Excited States, [1s ² 2s ² 2p ⁶ 3s ² 3p ⁵] n1, n=14	36
22. Computed Values of gA as a Function of Transition Wave- length (2 to 16 μm) for Argon Excited States, [1s ² 2s ² 2p ⁶ 3s ² 3p ⁵] n1, n=16	37
23. Computed Values of gA as a Function of Transition Wave- length (2 to 16 μm) for Argon Excited States, [1s ² 2s ² 2p ⁶ 3s ² 3p ⁵] n1, n=18	37

Illustrations

24. Computed Values of gA as a Function of Transition Wave-length (2 to 16 μm) for Argon Excited States, [1s ² 2s ² 2p ⁶ 3s ² 3p ⁵] n1, n=20	38
25. Computed Values of gA as a Function of Transition Wave-length (2 to 16 μm) for Argon Excited States, [1s ² 2s ² 2p ⁶ 3s ² 3p ⁵] n1, n=22	38
26a. Experimental COCHISE Argon Emission Spectrum, 8 to 16 μm	41
26b. Simulated Argon Spectrum, 8 to 16 μm	41
27a. Experimental COCHISE Argon Emission Spectrum, 11.90 to 12.50 μm	44
27b. Simulated Argon Spectrum, 11.90 to 12.50 μm	44
28. Observed ArI Transitions, 2 to 3.5 μm	46
29. Observed ArI Transitions, 4 to 7 μm	47
30. Observed ArI Transitions, 10 to 16 μm	48

Tables

1. Tentatively Identified Spectral Transitions for Argon Between 1.95 and 16.0 μm	25
2. Spectral Transitions: 8.50 to 10.00 μm	43

Accession For	
NTIS	GRA&I
DTIC TAB	<input type="checkbox"/>
Unannounced	<input type="checkbox"/>
Justification	
By _____	
Distribution/	
Availability Codes	
Dist	Avail and/or Special
A-1	



COCHISE Observations of Argon Rydberg Emission From 2 to 16 Micrometers

1. INTRODUCTION

Studies of the radiative and collisional properties of atomic Rydberg states have generated a rich literature for over 100 years.¹ A great many of the more recent experimental investigations have employed optical excitation methods to form highly excited states, and the bulk of the work in this area deals with alkali metals. Relatively little attention has been given to Rydberg state spectroscopy for more complex atoms such as O, N, and Ar, which are significant constituents of the upper atmosphere. Furthermore, in high-altitude electron bombardments, as in low-pressure laboratory electric discharges, Rydberg species can be formed by kinetic processes that might give rise to non-Boltzmann population distributions among the upper energy levels. Thus, it is informative to study the excitation of atmospheric species under laboratory conditions representative of the high altitude environment. We report here the first direct observations of long-wavelength infrared (LWIR) fluorescence from Rydberg states of Ar excited in a low-pressure microwave discharge, as studied in the COCHISE cryogenic infrared fluorescence facility.

(Received for publication 4 August 1983)

1. Feneuille, S., and Jacquinot, P. (1981) Atomic Rydberg states, Adv. Atomic Molec. Phys. 17:99.

Argon is a significant constituent in the thermosphere, having a vertical column density in excess of 10^{16} cm^{-2} at 100 km.² In a strong aurora, there may be sufficient excitation of high Rydberg levels of Ar to give rise to measurable line radiation in the infrared, where radiative lifetimes of such transitions are in the range 1 to 100 μs . In addition, Ar is a convenient bath gas for use in all COCHISE infrared chemiluminescence studies, and its spectral signature is present to some extent in all measurements. For these reasons we have conducted a detailed investigation of the Ar emission spectrum observed in COCHISE.

The principal objectives of this investigation are to characterize the Ar spectrum from 2 to 16 μm at the highest possible spectral resolution, and to identify as fully as possible the sources of the emission and the kinetic mechanism of the excitation. Our greatest interest lies in the spectral region beyond 8 μm , where the data are unique and exhibit an unusual spectral distribution peaking near 12 μm . To accomplish these goals, we (1) obtained considerable spectral data over a range of spectral resolution and discharge operating conditions; (2) compared the observed emissions to transitions predicted from optical selection rules; and (3) compared the data to simulated dipole-allowed spectra computed using transition probabilities estimated from the Coulomb approximation.

For Rydberg atoms in which a single electron is excited to an orbital of large principle quantum number, that is, near the point of ionization, the excited electron moves in a near-Coulombic field of essentially unit charge. Thus, the transition frequencies in Rydberg spectra are often represented in terms of a simple hydrogenic approximation. In COCHISE, we observe infrared transitions from states with principal quantum numbers $4 \leq n < 12$ ($20,000$ to $1,000 \text{ cm}^{-1}$ below the ionization limit). For these transitions, we find that the hydrogenic approximation does not apply, even if quantum defects are considered. Furthermore, for the lower values of n exhibited in the data, whose transitions predominate at shorter wavelengths ($\lambda < 5 \mu\text{m}$), we observe that certain optical selection rules break down, and that the Coulomb approximation is clearly inappropriate for predicting spectral intensities. Finally, the spectral distribution at long wavelengths suggests excitation of the emitting species via a cascade mechanism initiated by ionic recombination.

2. Jacchia, L.G. (1977) Thermospheric Temperature, Density, and Composition: New Models, Smithsonian Astrophysical Observatory Special Report 375.

2. EXPERIMENTAL OBSERVATIONS

The design and operation of the COCHISE facility have been described in detail elsewhere.³⁻¹⁰ In brief, the entire radiative environment of the experiment is maintained at a base temperature of ~20 K, which effectively eliminates background radiation within the 2 to 20- μm operating range of the apparatus. The detection system consists of a scanning grating monochromator and a liquid-helium-cooled Si:As detector. Reagent gases are introduced through temperature-controlled feed lines to the reaction cell shown in Figure 1. A flowing Ar mixture at ~1 Torr passes through four parallel microwave discharges (2450 MHz, 50 W) 1.1 cm ID, prior to expanding into a low-pressure (~3 mT), cryogenically pumped interaction volume. A counterflow gas enters the volume from the opposite side to combine with the discharged gas in a stagnation region near the axis of the cylindrical field-of-view of the detector. In some cases (for example, Reference 8), this interaction consists of a chemical reaction under nearly single-collision conditions. In other experiments, all the emission observed arises from processes occurring in the discharge sidearms.^{3, 10}

In typical COCHISE chemiluminescence experiments, Ar acts as a carrier gas for small (<10 percent) flows of reagents, for example, N₂ or O₂, which are to be excited in the microwave discharges. Such conditions typically employ Ar

3. Rawlins, W. T., Caledonia, G. E., and Kennealy, J. P. (1981) Observation of spectrally resolved infrared chemiluminescence from vibrationally excited O₃(ν_3). *J. Geophys. Res.* 86:5247.
4. Rawlins, W. T., Piper, L. G., Green, B. D., Wilemski, G., Goela, J. S., and Caledonia, G. E. (1980) LABCEDE and COCHISE Analysis II, Vol. I (Final Report) PSI-TR 207A, Physical Sciences Inc., Andover, Mass.
5. Rawlins, W. T., Piper, L. G., Caledonia, G. E., and Green, B. D. (1981) COCHISE Research, PSI-TR 298, Physical Sciences Inc., Andover, Mass.
6. Rawlins, W. T., Murphy, H. C., Taylor, R. L., and Caledonia, G. E. (1980) Final Report on COCHISE Refurbishment, PSI-TR 222, Physical Sciences Inc., Andover, Mass.
7. Kennealy, J. P., DelGreco, F. P., Caledonia, G. E., and Rawlins, W. T. (1979) COCHISE: Laboratory spectroscopic studies of atmospheric phenomena with high-sensitivity cryogenic instrumentation, G. A. Vanesse, Ed., Proc. Soc. Photo-Opt. Instrum. Eng. 191:151.
8. Kennealy, J. P., DelGreco, F. P., Caledonia, G. E., and Green, B. D. (1978) Nitric oxide chemiexcitation occurring in the reaction between metastable nitrogen atoms and oxygen molecules, *J. Chem. Phys.* 69:1574.
9. Caledonia, G. E., Green, B. D., Simons, G. A., Kennealy, J. P., Robert, F. X., Corman, A., and DelGreco, F. P. (1977) COCHISE Studies I: Fluid Dynamical and Infrared Spectral Analyses, AFGL-TR-77-0281, AD A053218.
10. Rawlins, W. T., and Armstrong, R. A. (1982) COCHISE Observations of O₃ Formed by Three-Body Recombination of O and O₂, AFGL-TR-82-0273, AD A123653.

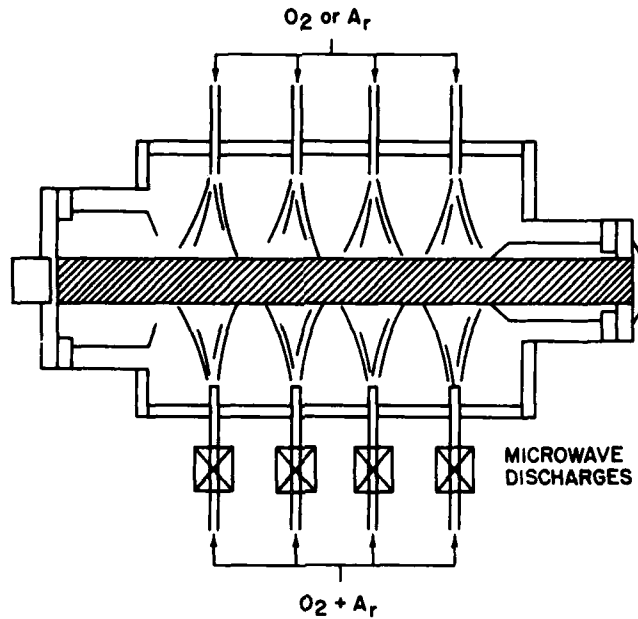


Figure 1. COCHISE Reaction Chamber. The cross-hatched region delineates the field-of-view of the detector (not shown)

pressures and flow rates of ~ 1 Torr and $640 \mu\text{mol s}^{-1}$, respectively, which give residence times of ~ 2 ms in the chemically active portion of the discharge. The Ar spectral studies reported here were carried out for pure Ar (Matheson, UHP) at discharge pressures of 0.1 to 2 Torr and temperatures of 80 to 150 K. The approximate discharge residence times ranged from 5 ms at 0.1 Torr to 0.8 ms at 2 Torr. For all conditions, a large number of sharp spectral features, apparently atomic lines and multiplets, were observed between 2 and $16 \mu\text{m}$.

The observed intensities and spectral distributions are insensitive to the flow rate and identity of the counterflow gas. This indicates that the emission arises not from the field-of-view but from the discharge tubes themselves, and reaches the field-of-view by multiple reflections within the reaction chamber. This is consistent with our expectation that the emitting species can be excited only in the active discharge and that their radiative lifetimes (~ 1 to $10 \mu\text{s}$ for atoms) would be much shorter than the ~ 0.5 -ms transit time from the end of the discharge tubes to the detector's field-of-view. We expect the reduction in the initial line intensities due to the multiple reflections is at least 3 orders of magnitude (that is, of order 10 reflections). This means that we can observe only the most intense features of the many that must arise from such discharges, that is, primarily those of neutral Ar.

The scattering of the light introduces a severe restriction into the interpretation of absolute and relative intensities. For typical chemiluminescence experiments in COCHISE, in-situ blackbody calibrations permit determinations of the absolute and relative responsivity of the optical system for radiation arising from the central interaction volume. These calibrations have been applied to the observed Ar spectra, but they are not strictly valid for scattered light. We anticipate that the reflectivity of the copper wall of the reaction chamber varies relatively weakly and uniformly with wavelength, so that relative intensities over small wavelength intervals (a few μm) are reasonably representative of those emanating from the discharge. A notable exception occurs near $7 \mu\text{m}$, below which the sapphire walls of the discharge tubes will transmit the plasma radiation, possibly giving artificially large intensities relative to those at longer wavelengths. We present our observed intensities in arbitrary units proportional to $\text{W/cm}^{-2} \text{ sr}^{-1} \mu\text{m}^{-1}$ (as determined by the blackbody calibrations) to give a measure of the apparent relative intensity on a consistent scale.

Low-resolution survey spectra of the observed Ar-related emission are shown in Figures 2 to 4. In general, there are many intense features from 2 to $5 \mu\text{m}$, a striking "window" between 5 and $10 \mu\text{m}$, and several moderately strong features from 10 to $15 \mu\text{m}$. The general appearance of this spectrum is insensitive to pressure and temperature, although the total spectral intensity diminishes as the pressure is increased (Figure 5). In general, as N_2 or O_2 are admitted to the discharge, the intensities of Ar-related emissions decrease. This is shown for the case of O_2 in Figure 6. The observed signal actually passes through a maximum near 1 percent O_2 , suggesting the possibility of oxygen-related emissions within the $\sim 0.08\text{-}\mu\text{m}$ (FWHM) bandpass of the measurement; unfortunately, low S/N ratios have thus far prevented high-resolution scans for these discharge conditions. The decrease in signal upon further O_2 addition is likely due to quenching of the emission by O or O_2 . The pressure effect shown in Figure 5 is difficult to interpret because changing the Ar pressure in the discharge sidearms simultaneously alters the flow velocity (that is, the residence time) and the E/N in the discharge plasma, as well as other characteristics of the discharge.

Most of the detailed spectral studies were carried out at 0.1 Torr, where the S/N ratios were the most favorable. Example spectral scans at medium and high spectral resolution are shown in Figures 7 to 12. All the features exhibit spectral characteristics typical of atomic lines or multiplets; in addition, many of the line groupings cannot be separated even at the highest resolution possible for these measurements.

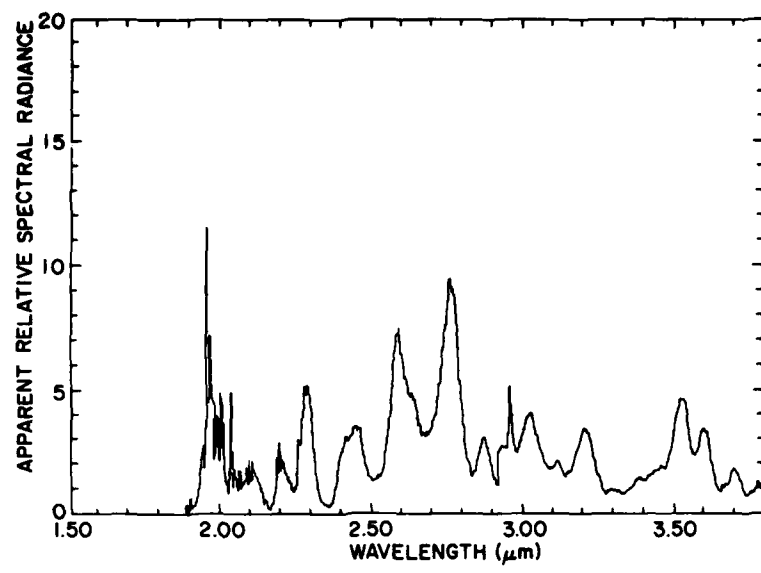


Figure 2. Survey of Ar SWIR Emission, 0.04- μm Resolution,
0.1 Torr

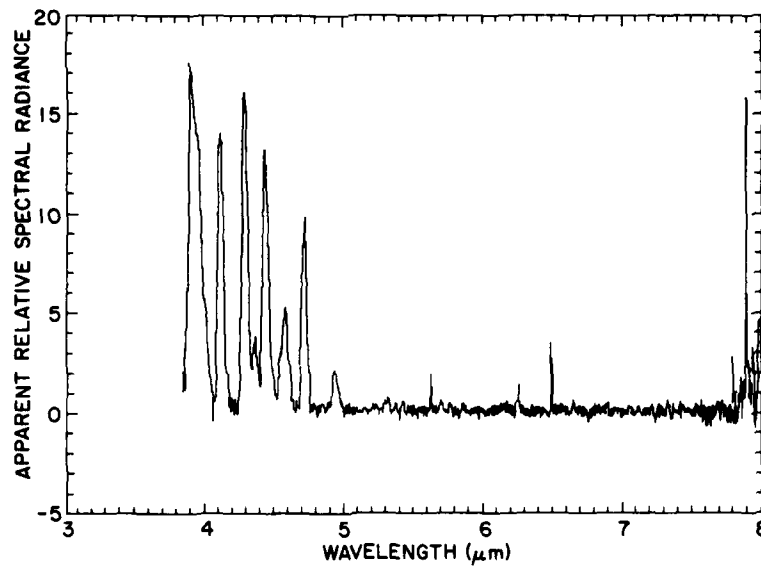


Figure 3. Survey of Ar MWIR Emission, 0.04- μm Resolution,
0.1 Torr

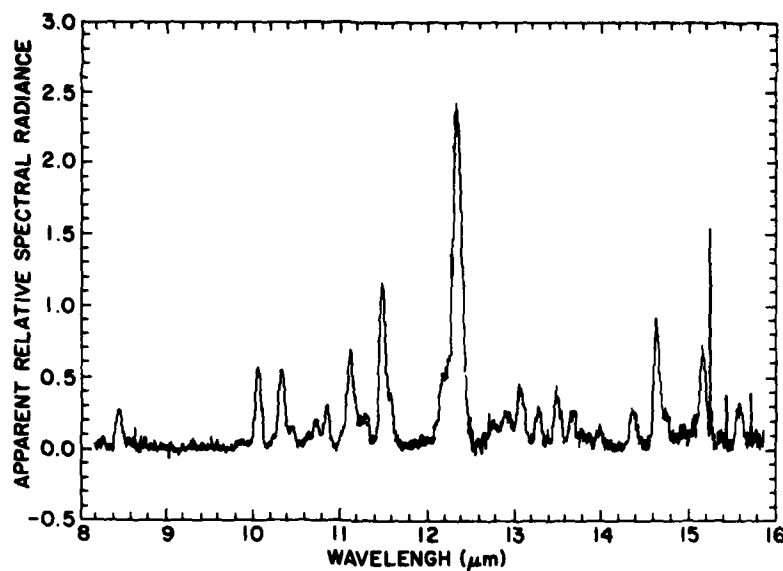


Figure 4. Survey of Ar LWIR Emission, 0.08- μm Resolution,
0.1 Torr

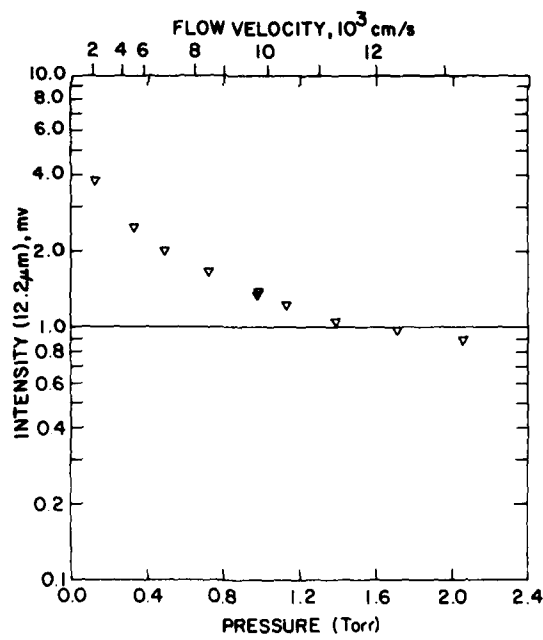


Figure 5. ArI Intensity at 12.2 μm as a Function
of Total Ar Pressure in Discharge Sidearms.
Discharge gas is 100 percent Ar; no counterflow

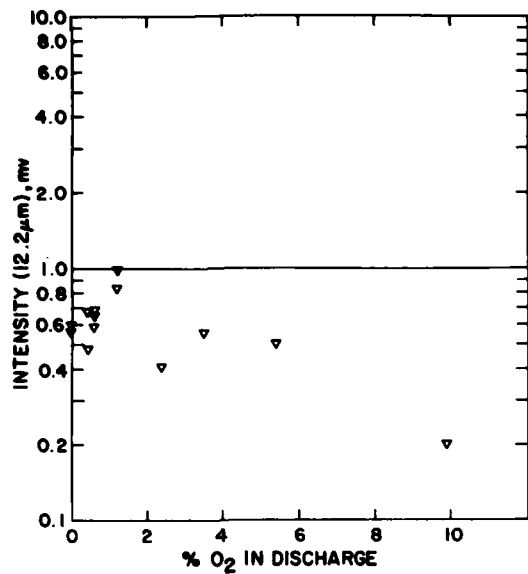


Figure 6. ArI Intensity at $12.2 \mu\text{m}$ as a Function of O_2 Level in the Discharge Tubes, $P_{\text{Ar}} = 1.3 \text{ Torr}$

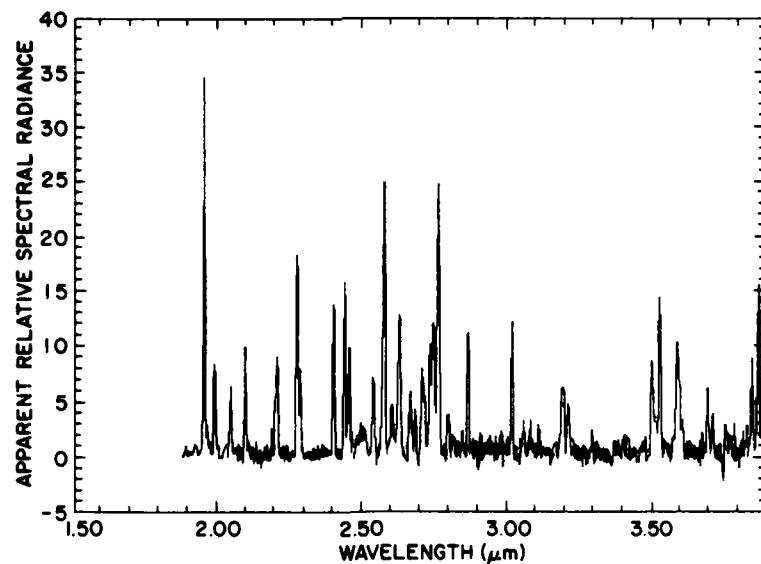


Figure 7. High Resolution Spectrum of Ar Emission From 2 to $4 \mu\text{m}$, $0.007\text{-}\mu\text{m}$ Resolution, 0.1 Torr

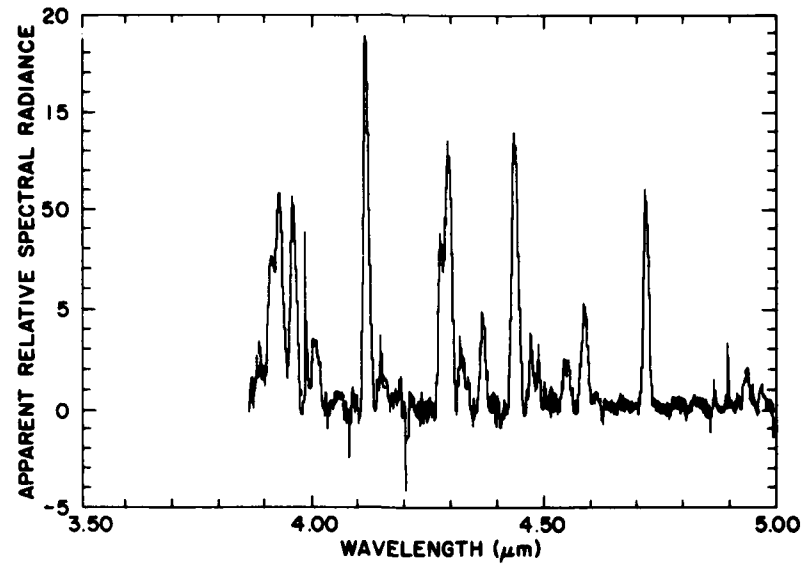


Figure 8. Medium Resolution Spectrum of Ar Emission,
4 to 5 μm , 0.013- μm Resolution, 0.1 Torr

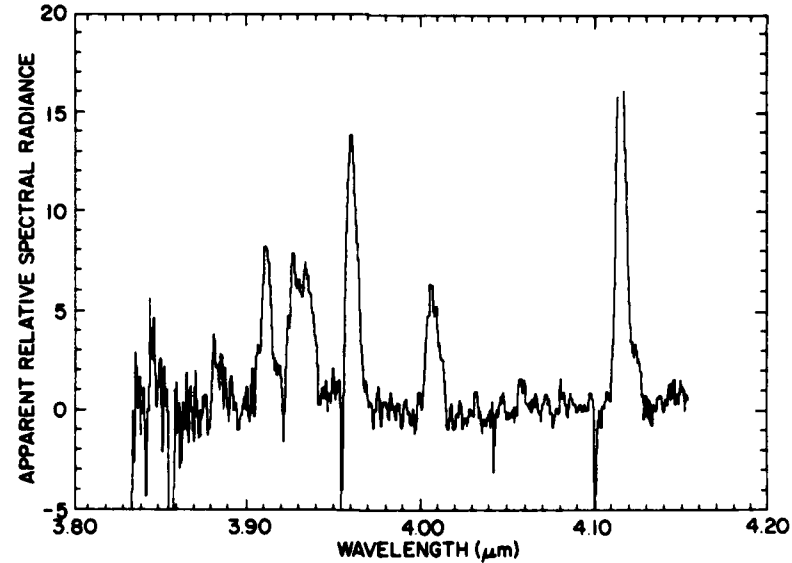


Figure 9. High Resolution Spectrum of Ar Emission Near 4 μm ,
0.007- μm Resolution, 0.1 Torr. The peak near 4.12 μm is off scale

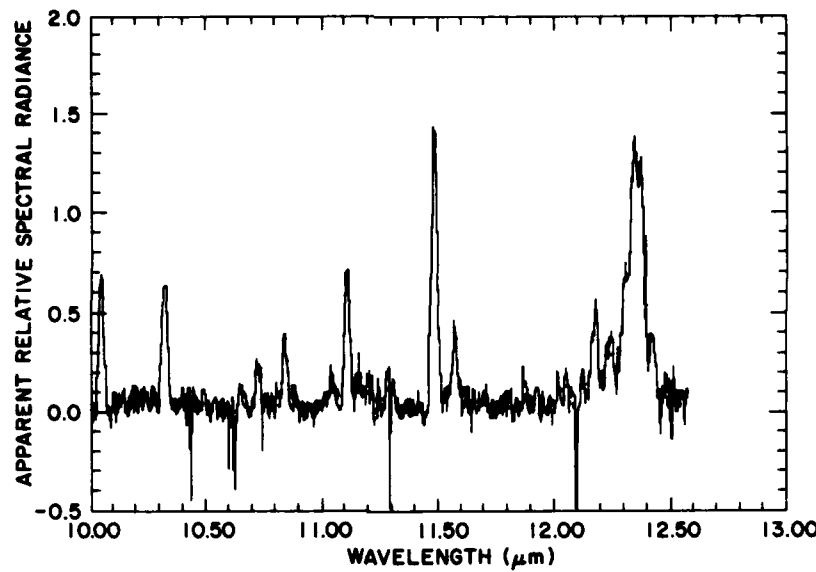


Figure 10. Medium Resolution Spectrum of Ar Emission,
10 to 12 μm , 0.027- μm Resolution, 0.1 Torr

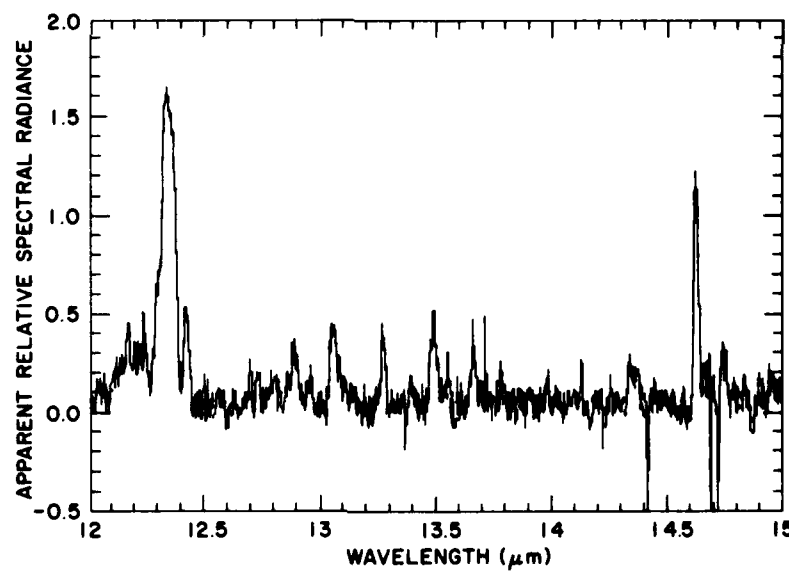


Figure 11. Medium Resolution Spectrum of Ar Emission,
12 to 15 μm , 0.027- μm Resolution, 0.1 Torr

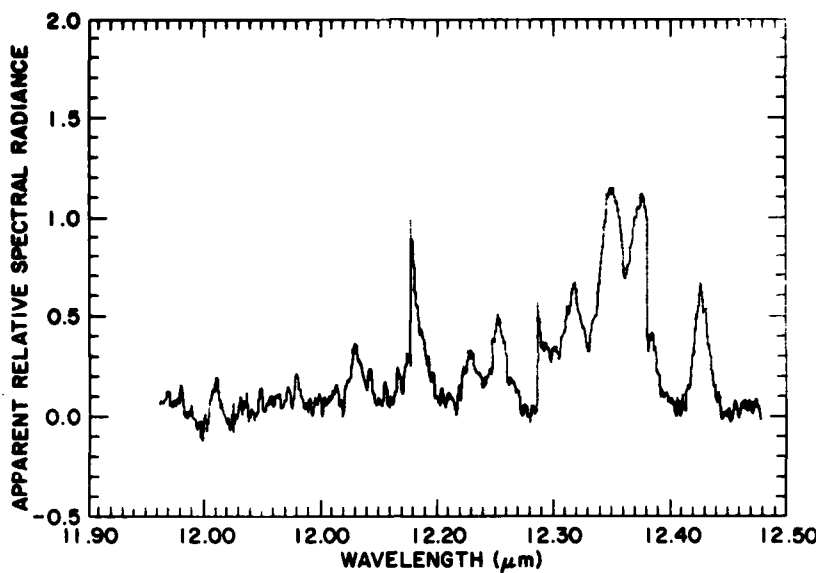


Figure 12. High Resolution Spectrum of Ar Emission Near 12.3 μm , 0.013- μm Resolution, 0.1 Torr

The probable sources of this emission are Rydberg states of Ar or Ar^+ excited in the discharge. However, the levels of excitation in such discharges are rather low ($[\text{e}^-] \sim 10^{11} \text{ cm}^{-3}$, average electron energy $\sim 2 \text{ eV}$),¹¹ so the total Ar^+ number density is several orders of magnitude smaller than that of the neutral atom. Thus, the observed transitions appear to arise from high Rydberg-like energy levels of neutral Ar. However, since the spectroscopic literature does not extend beyond $\sim 4 \mu\text{m}$, considerable analysis is required to make the spectral assignments. The Rydberg series of hydrogen-like, $n \rightarrow n - 1$ transitions, which should appear in the spectra of all highly excited atomic gases, is given by

$$\lambda = 0.09113 \frac{n^2(n-1)^2}{2n-1} \text{ ,}$$

where λ is the line position in μm and n is the principle quantum number of the emitting state ($n \geq 5$). The first few lines, for $n = 4, 5, 6, 7, \dots$, are at 4.05, 7.46, 12.36, 19.05, ... μm , respectively. However, these are idealized lines which are most closely approximated by transitions involving states with large

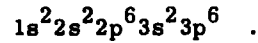
11. Kaufman, F. (1969) The production of atoms and simple radicals in glow discharges, Adv. Chem. Ser. 80:29.

orbital angular momentum (high ℓ -values); other transitions at nearby wavelengths may be expected for Rydberg states with lower ℓ or spin-orbit coupling. The Rydberg wavelengths of 4.05 and 12.36 μm correlate well with the strong transitions we observe at ~ 4.0 and 12.3 μm ; however, the 7.46- μm transition is conspicuously absent from the observed spectra. Furthermore, the observed spectra are clearly complex and contain many strong transitions in addition to those near 4 and 12 μm . Indeed, even the 4- and 12- μm features are extremely complex when examined under high resolution (refer to Figures 9 and 12). Thus, in order to interpret the spectral data, it is necessary to predict all possible transitions according to the energy levels and optical selection rules for Ar, and to estimate transition probabilities in order to compare the experimental spectra to simulated spectra convolved with the instrumental resolution function.

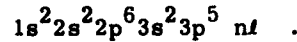
3. INFRARED SPECTROSCOPY OF ArI

3.1 Argon Rydberg States

The ground state configuration of the Ar atom is given by



The lowest-lying excited states are formed by promoting a p electron to an outer shell to give configurations of the form



These states are split into two groups of levels depending on the state of the core electrons. The core electrons form two different configurations, $^2P_{1/2}$ and $^2P_{3/2}$, which couple to the outer electron to give the atomic configuration.

The excited states are described using the intermediate or j - ℓ coupling scheme. Specific states are denoted as



where

$$K = \ell + j_c \quad \text{and} \quad J = K + S .$$

K is the resultant angular momentum formed by coupling the core electron angular momentum j_c to the outer electron orbital angular momentum. Primed states denote $j_c = 1/2$ and unprimed states denote $j_c = 3/2$. J is the total atomic momentum formed by coupling the outer electron spin angular momentum, S , to K . A superscript zero is used to denote state of even orbital angular momentum ($\ell = s, d, g$). The primed and unprimed manifolds rapidly divide with increasing n into two distinct groups of levels. The $j_c = 1/2$ manifold approaches in its ionization limit the $^2P_{1/2}$ states of the Ar ion; $j_c = 3/2$ approaches the $^2P_{3/2}$ state ion. The respective ionization limits of the $j_c = 3/2$ and $j_c = 1/2$ manifolds are 127109.9 cm^{-1} and 128541.3 cm^{-1} . Energy level tables have been compiled by Moore¹² and more recently by Bashkin and Stoner.¹³

A simplified energy diagram for lowest Ar excited states is shown in Figure 13. The states are labeled by principal quantum number, n . The energy span for states of given n and ℓ is depicted by a vertical line. States belonging to the $^2P_{1/2}$ core are marked with a prime. Two sets of states, $4s$ and $4s'$, are below the scale of the figure and therefore are not shown. One immediate observation is the rather drastic compression of states for higher principal quantum numbers. A more detailed level diagram is given by Bashkin and Stoner.¹³

3.2 Calculation of Radiative Transition Probabilities

We shall summarize the calculation of radiative transition probabilities within the framework of a one-electron dipole approximation. The selection rules that result for the transition between states $n_1 \ell_1 [K_1] J_1$ and $n_2 \ell_2 [K_2] J_2$ are:

$$\ell_1 - \ell_2 = \pm 1$$

$$K_1 - K_2 = 0 (K_1 \neq 0), \pm 1$$

$$J_1 - J_2 = 0 (J_1 \neq 0), \pm 1$$

$$j_{c_1} - j_{c_2} = 0 . \quad (1)$$

12. Moore, C.E. (1971) Atomic Energy Levels, Vol. 1, NSRDS-NBS35.

13. Bashkin, S., and Stoner, J.O., Jr. (1978) Atomic Energy - Level and Grotrian Diagrams 2, North-Holland Publishing Co., New York.

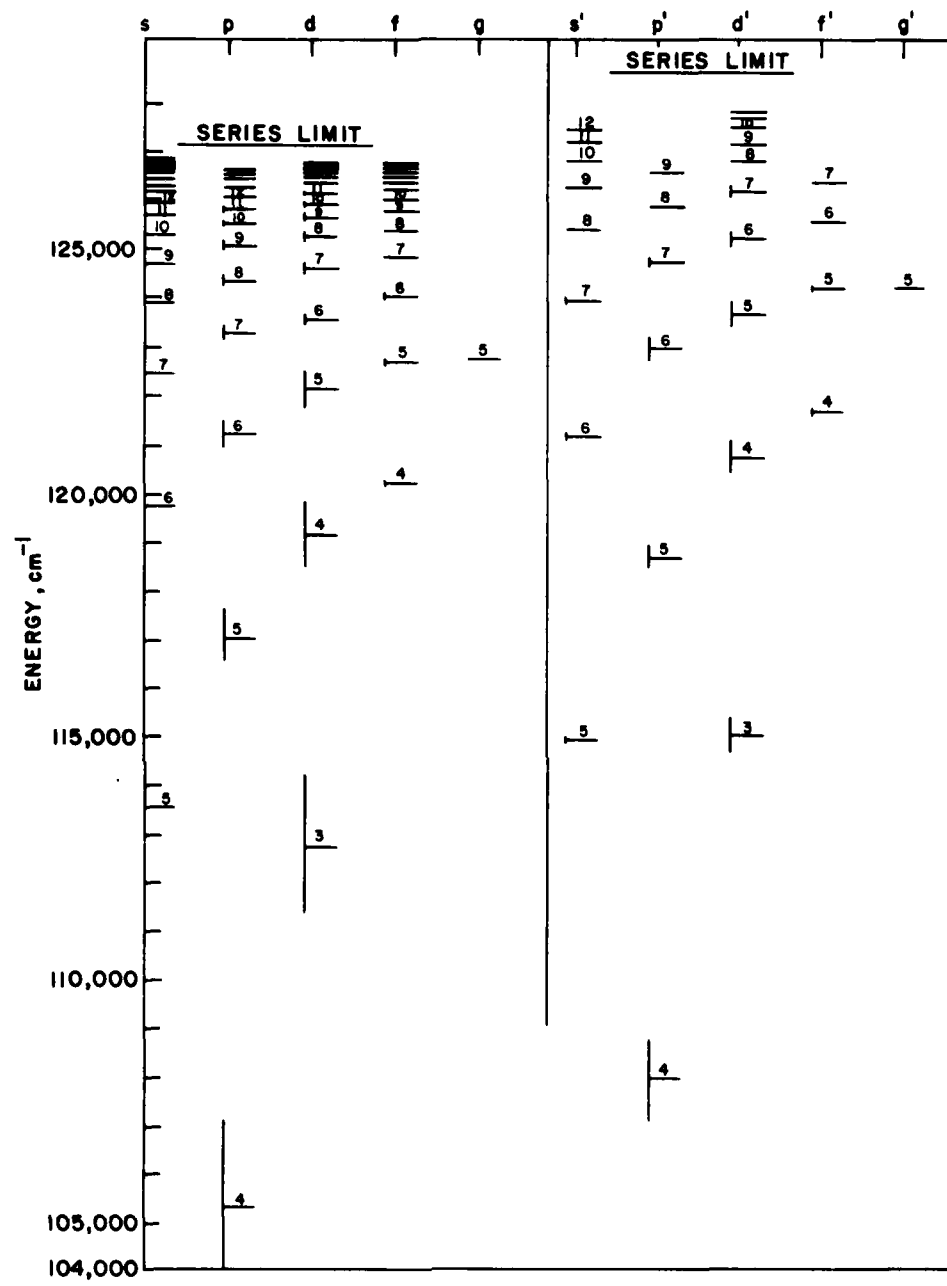


Figure 13. Energy Level Diagram for Rydberg States of Argon. Series limits for $^2P_{1/2}$ (primed) and $^2P_{3/2}$ (unprimed) core states are shown

The computed line strength is given by

$$S = \frac{1}{3} (2J_1 + 1)(2J_2 + 1)(2K_1 + 1)(2K_2 + 1) \\ \cdot \left\{ \begin{matrix} J_1 & J_2 & 1 \\ K_2 & K_1 & 1/2 \end{matrix} \right\}^2 \left\{ \begin{matrix} \ell_2 & K_2 & j_c \\ \ell_1 & \ell_1 & 1 \end{matrix} \right\}^2 | \langle \ell_1 || T || \ell_2 \rangle |^2 . \quad (2)$$

where the bracketed quantities are 6-j symbols and $\langle \ell_1 || T || \ell_2 \rangle$ is a reduced matrix element of the dipole operator. It is expressed as the following:

$$| \langle \ell_1 || T || \ell_2 \rangle |^2 = \frac{3}{4\pi} (2\ell_1 + 1)(2\ell_2 + 1) C(\ell_1 \ell_2; 000)^2 \\ \times \left| \int_0^\infty f_{\ell_1}(r) f_{\ell_2}(r) r dr \right|^2 , \quad (3)$$

where $C(\ell_1, \ell_2; 000)$ is a Clebsch-Gordan coefficient and $f_{\ell_1}(r)$ and $f_{\ell_2}(r)$ are radial wave functions for the outer electron. We will use the Coulomb approximation for the evaluation of the radial integral.

In the Coulomb approximation the radial wave functions are approximated by hydrogenic wave functions, that is,

$$I \equiv \int_0^\infty f_{\ell_1}(r) f_{\ell_2}(r) r dr \approx \int_0^\infty \phi_{\ell_1}^{\text{coul}}(r) \phi_{\ell_2}^{\text{coul}}(r) r dr , \quad (4)$$

where $\phi_{\ell}^{\text{coul}}$ is a hydrogenic wave function. Several methods of evaluation of I are available.

Bates and Damgaard¹⁴ and others^{15, 16} have presented an analytic expression for I:

-
- 14. Bates, D. R., and Damgaard, A. (1949) The calculation of the absolute strengths of spectral lines, Phil. Trans. Roy. Soc. A242:101.
 - 15. Statz, H., Tang, C. L., and Koster, G. F. (1963) Approximate electromagnetic transition probabilities and relative electron excitation cross sections for rare-gas masers, J. Appl. Phys. 34:2625.
 - 16. Koster, G. F., and Statz, H. (1964) Probabilities for the neon laser transitions, J. Appl. Phys. 35:2654.

$$I = \frac{2^{n_1+n_2}}{(n_1+1)(n_2+1)} [\Gamma(n_1+l_1+1)\Gamma(n_1-l_1)\Gamma(n_2+l_2+1)\Gamma(n_2-l_2)]^{-1/2} \\ \times \sum_{k_1=0}^{\infty} \sum_{k_2=0}^{\infty} a_{k_1} a_{k_2} \left[\frac{n_1 n_2}{(n_1+n_2)} \right]^{n_1+n_2+2-k_1-k_2} \Gamma(n_1+n_2+2-k_1-k_2) . \quad (5)$$

The principal quantum numbers n_1 and n_2 are non-integers and are evaluated for each state from the following relation

$$n = \left(\frac{109737}{E_\infty - E} \right)^{1/2} , \quad (6)$$

where E_∞ is the ionization limit (cm^{-1}) of the state manifold and E is the term value (cm^{-1}) of the state. The coefficients a_{k_1} and a_{k_2} are evaluated from the recurrence relation

$$a_k = \frac{na_{k-1}}{2k} [l(l+1) - (n-k)(n-k+1)] , \quad (7)$$

with $a_0 = 1$ for each set of coefficients. The summation is truncated by the condition $k_1 + k_2 < n_1 + n_2 - 1$. This procedure is computationally very rapid and works well for $n_1 + n_2 < 18$, using double precision arithmetic. The problem at higher principal effective quantum numbers arises from cancellation between large numbers in the summation to give smaller final results. For higher effective principal quantum numbers we use the method of Katterbach.¹⁷

Katterbach uses a semi-numerical procedure in which I is approximated as:

$$I = \int \phi_{l_1}^{\text{coul}}(r) \phi_{l_2}^{\text{coul}}(r) r dr \approx \Delta r \sum_{\nu=0}^{\nu_{\max}} \phi_{l_1}^{\text{coul}}(r_\nu) \phi_{l_2}^{\text{coul}}(r_\nu) . \quad (8)$$

17. Friedrich, H., Katterbach, K., and Trefftz, E. (1970) On the accuracy of machine programs for calculating oscillator strengths by Coulomb approximation, J. Quant. Spectrosc. Trans. 10:11.

The hydrogenic wave functions are approximated as

$$\phi_l^{\text{coul}}(r) = \frac{1}{[n^2 \Gamma(n+l+1) \Gamma(n-l)]^{1/2}} \left(\frac{2r}{n}\right)^n e^{-r/\nu} \sum_{t=0}^{t_{\max}} a_t r^{-t} \quad (9)$$

with t_{\max} determined by the inequality

$$t_{\max} \leq n + 1 \leq t_{\max} + 1$$

and the a_t defined as in the Bates-Damgaard method. The step size Δr is generally taken to be 0.125. Larger values, $\Delta r = 0.30$, give identical results for the cases studied. The starting point r_0 is taken to be 0.25. The value of ν_{\max} is determined by the relation

$$\frac{|\phi_l^{\text{coul}}(r_{\nu_{\max}})|}{\max |\phi_l^{\text{coul}}(r)|} \leq e^{-13} \quad (10)$$

for the wavefunction with the smaller principal quantum number.

We have found that these two methods give virtually identical results in cases when comparison is possible. The Bates-Damgaard method is more computationally efficient and therefore used when applicable. Other cases were computed using Katterbach's method.

The Einstein coefficient, A, of the emitting species is inversely proportional to its radiative lifetime. These coefficients are related to the wavelength-independent atomic linestrengths, S, by the relationship

$$gA = \frac{2.026 \times 10^{-6}}{\lambda^3} \times S \quad , \quad (11)$$

where λ is the transition wavelength given in centimeters and g the degeneracy of the radiating state.

We have computed gA factors for radiating states from $n = 4$ to $n = 22$ for transitions between 2 and 16 μm . Additionally, simulations of radiation from hot Ar gas have been computed. The results of these calculations are presented in the next section.

4. RESULTS OF SPECTRAL ANALYSIS

In Table 1 we list tentatively identified Rydberg transitions. For most observed spectral features more than one transition is given. This is a consequence of the large density of spectral lines for excited Ar and limited spectral resolution to discriminate between the various transitions. The possible transitions were determined using a weaker set of selection rules than those previously discussed for spectral computations. For the weaker selection rules the restriction of core angular momentum invariance is dropped, hence transitions between the $^2P_{1/2}$ and $^2P_{3/2}$ manifolds are allowed. Experimentally these transitions are found to be important at shorter wavelengths, for example, Humphreys¹⁸ notes many core changing transitions, several quite intense, in his compilation of observed Ar lines between 1.2 and 4.0 μm .

Table 1 includes the observed peak wavelength, identified possible transitions, and predicted wavelength based on the state energies listed in Moore's¹² and Bashkin and Stoner's¹³ tables. An "H" after the listing indicates that the transition is listed in Humphreys' compilation.¹⁸ Table 1 includes the entire range of the present spectral measurements, from approximately 2.0 to 16.0 μm .

Some general conclusions about the types of identified transitions may be made. There is a general tendency to see radiation from higher energy states, that is, higher principal quantum numbers, at longer wavelengths. This seems reasonable since the energy gaps are too large for low quantum numbers to radiate in the LWIR. However, with the exception of the peaks observed around 12.2 to 12.4 μm (and to some extent around 2.4 μm) it is rarely necessary to invoke states of quantum numbers greater than eight. Two possible explanations are that excited state Ar formation does not produce such states or that such states, which have larger radiative lifetimes, are quenched by gas phase or wall collisions.

A second point is that, as mentioned above, core changing transitions are quite important at shorter wavelengths. Several peaks seem to be directly attributable to such transitions: 2.100, 2.212, 2.445, 2.634, and 4.116 μm . The significance of such transitions makes the use of the Coulomb approximation rather dubious since they are beyond the scope of that treatment. It seems that for longer wavelengths (8 to 16 μm) core changing transitions play a less significant role. The Coulomb approximation may, therefore, be more reliable for longer wavelength radiation. (The 12.2 to 12.4 μm feature is an exception.) This conclusion is also physically appealing since for higher quantum numbers the outer electrons become more "hydrogen-like".

18. Humphreys, C.J. (1974) First spectra of neon, argon and xenon 136 in the 1.2-4.0 μm region, J. Phys. Chem. Ref. Data 2:519.

Table 1. Tentatively Identified Spectral Transitions for Argon
Between 1.95 and 16.0 μm

Observed Peak Wavelength (μm)	Transition	Predicted Wavelength (μm)	
1.960	$5\text{d}'[5/2]_2^0 \rightarrow 5\text{p}'[3/2]_1$	1.9616	H
	$5\text{d}'[5/2]_2^0 \rightarrow 5\text{p}[3/2]_2$	1.9614	H
1.995	$5\text{p}[3/2]_1 \rightarrow 3\text{d}[3/2]_2^0$	1.9950	H
2.050	$6\text{d}'[3/2]_2^0 \rightarrow 4\text{f}[3/2]_2$	2.0501	
	$6\text{d}'[3/2]_2^0 \rightarrow 4\text{f}[3/2]_1$	2.0500	
	$6\text{f}'[7/2]_3 \rightarrow 4\text{d}'[3/2]_2^0$	2.0484	
	$6\text{f}'[5/2]_3 \rightarrow 4\text{d}'[3/2]_2^0$	2.0483	
	$6\text{f}'[5/2]_2 \rightarrow 4\text{d}'[3/2]_2^0$	2.0482	
2.100	$3\text{d}[1/2]_1^0 \rightarrow 4\text{d}[1/2]_0$	2.0992	H
	$5\text{p}'[3/2]_1 \rightarrow 5\text{s}[3/2]_1^0$	2.0989	H
2.212	$3\text{d}[1/2]_1^0 \rightarrow 4\text{p}'[3/2]_2$	2.2083	H
	$5\text{p}[1/2]_1 \rightarrow 3\text{d}[3/2]_2^0$	2.2119	H
2.280	$7\text{d}[7/2]_4^0 \rightarrow 4\text{f}[5/2]_3$	2.283	
2.290	$5\text{d}[1/2]_1^0 \rightarrow 5\text{p}[1/2]_0$	2.2883	
	$6\text{f}[5/2]_2 \rightarrow 4\text{s}[3/2]_2^0$	2.2892	H
	$6\text{f}[5/2]_3 \rightarrow 6\text{s}[3/2]_2^0$	2.2891	H
	$7\text{d}[1/2]_1^0 \rightarrow 4\text{f}[3/2]_1$	2.2902	
	$7\text{d}[1/2]_1^0 \rightarrow 4\text{f}[3/2]_2$	2.2901	
	$9\text{d}[3/2]_1^0 \rightarrow 6\text{p}[3/2]_2$	2.2898	

Table 1. Tentatively Identified Spectral Transitions for Argon
Between 1.95 and 16.0 μm (Contd)

Observed Peak Wavelength (μm)	Transition	Predicted Wavelength (μm)
2.406	$5\text{p}[3/2]_2 \rightarrow 3\text{d}[3/2]_3^0$	2.4021
	$6\text{s}'[1/2]_1^0 \rightarrow 5\text{p}'[5/2]_2$	2.4027
	$8\text{s}'[1/2]_1^0 \rightarrow 6\text{p}[5/2]_2$	2.4030
2.445	$6\text{p}'[1/2]_1 \rightarrow 4\text{d}[1/2]_0^0$	2.4455
	$6\text{d}'[3/2]_1^0 \rightarrow 6\text{p}[5/2]_2$	2.4424
2.462	$9\text{p}[3/2]_1 \rightarrow 4\text{d}'[3/2]_1^0$	2.4627
	$9\text{p}[3/2]_2 \rightarrow 4\text{d}'[3/2]_1^0$	2.4613
	$10\text{s}[3/2]_1^0 \rightarrow 6\text{p}[3/2]_2$	2.4623
2.544	$13\text{p}[3/2]_2 \rightarrow 5\text{d}[5/2]_3^0$	2.5460
	$5\text{p}[1/2]_0 \rightarrow 5\text{s}[3/2]_1^0$	2.5505
2.582	$5\text{d}[5/2]_2^0 \rightarrow 5\text{p}'[3/2]_1$	2.5809
	$6\text{d}'[3/2]_2^0 \rightarrow 6\text{p}[5/2]_2$	2.5809
	$6\text{d}'[5/2]_3^0 \rightarrow 6\text{p}[3/2]_2$	2.5778
	$8\text{d}[1/2]_1^0 \rightarrow 6\text{p}[3/2]_1$	2.5782
	$8\text{s}'[1/2]_1^0 \rightarrow 6\text{p}[1/2]_0$	2.5753
	$9\text{d}'[3/2]_2^0 \rightarrow 7\text{p}[3/2]_1$	2.5800
	$9\text{d}'[3/2]_1^0 \rightarrow 7\text{p}[3/2]_1$	2.5800
	$5\text{p}'[1/2]_0 \rightarrow 5\text{s}'[1/2]_1^0$	2.5661
	$6\text{d}'[3/2]_2^0 \rightarrow 6\text{p}[3/2]_2$	2.6345
2.634	$4\text{d}'[5/2]_3^0 \rightarrow 4\text{p}[5/2]_3$	2.6235
	H	

Table 1. Tentatively Identified Spectral Transitions for Argon
Between 1.95 and 16.0 μm (Contd)

Observed Peak Wavelength (μm)	Transition	Predicted Wavelength (μm)	
2.672	$5\text{p}'[3/2]_1 \rightarrow 3\text{d}'[5/2]_2^0$	2.6543	H
	$5\text{p}[3/2]_2 \rightarrow 3\text{d}[5/2]_2^0$	2.6605	H
2.690	$5\text{p}[3/2]_2 \rightarrow 5\text{s}[3/2]_2^0$	2.6917	H
2.715	$5\text{p}[3/2]_1 \rightarrow 5\text{s}[3/2]_2^0$	2.7152	H
	$5\text{f}[5/2]_3 \rightarrow 4\text{d}[7/2]_4^0$	2.7142	
2.721	$4\text{d}'[5/2]_2^0 \rightarrow 5\text{p}[5/2]_3$	2.7202	
	$5\text{f}[9/2]_4 \rightarrow 4\text{d}[7/2]_4^0$	2.7233	
2.740	$5\text{p}'[3/2]_2 \rightarrow 3\text{d}'[5/2]_3^0$	2.7419	
	$5\text{p}'[1/2]_0 \rightarrow 3\text{d}'[3/2]_2^0$	2.7364	H
2.750	$6\text{d}[5/2]_2^0 \rightarrow 4\text{f}[3/2]_2$	2.7486	
	$6\text{d}[5/2]_2^0 \rightarrow 4\text{f}[3/2]_1$	2.7483	
	$7\text{p}'[1/2]_1 \rightarrow 4\text{d}'[3/2]_1^0$	2.7480	
	$7\text{p}[5/2]_3 \rightarrow 4\text{d}[5/2]_3^0$	2.7475	
2.769	$7\text{s}[3/2]_1^0 \rightarrow 5\text{p}'[1/2]_0$	2.7712	
2.870	$5\text{f}[9/2]_4 \rightarrow 4\text{d}[7/2]_3^0$	2.8713	H
	$5\text{p}'[1/2]_1 \rightarrow 5\text{s}'[1/2]_1^0$	2.8698	H
	$7\text{p}'[3/2]_1 \rightarrow 6\text{s}'[1/2]_1^0$	2.8718	
	$7\text{d}[7/2]_3^0 \rightarrow 6\text{p}[5/2]_3$	2.8702	
	$7\text{d}[1/2]_1^0 \rightarrow 6\text{p}[1/2]_1$	2.8685	

Table 1. Tentatively Identified Spectral Transitions for Argon
Between 1.95 and 16.0 μm (Contd)

Observed Peak Wavelength (μm)	Transition	Predicted Wavelength (μm)	
3.022	$5\text{d}'[5/2]_3^0 \rightarrow 4\text{f}[7/2]_4$	3.0236	
	$5\text{d}'[7/2]_3^0 \rightarrow 4\text{f}[7/2]_3$	3.0236	
	$9\text{f}[7/2]_{3,2} \rightarrow 7\text{s}[3/2]_2^0$	3.0223	
3.194	$5\text{f}[9/2]_4 \rightarrow 4\text{d}[5/2]_3^0$	3.1953	H
3.200	$5\text{f}'[7/2]_2 \rightarrow 4\text{d}'[3/2]_1^0$	3.1995	H
3.205	$5\text{f}[3/2]_2 \rightarrow 4\text{d}[5/2]_3^0$	3.2048	H
3.217	$8\text{f}[5/2]_3 \rightarrow 5\text{d}[5/2]_2^0$	3.2166	
3.505	$5\text{p}[5/2]_2 \rightarrow 3\text{d}[3/2]_1^0$	3.5068	H
3.531	$7\text{f}[5/2]_3 \rightarrow 5\text{d}[7/2]_4^0$	3.5349	
	$7\text{f}[7/2]_{3,4} \rightarrow 5\text{d}[7/2]_4^0$	3.5302	
	$8\text{s}[3/2]_2^0 \rightarrow 6\text{p}[1/2]_1$	3.5280	
3.593	$4\text{d}[5/2]_2^0 \rightarrow 5\text{p}[1/2]_1$	3.5909	
3.697	$7\text{f}[5/2]_3 \rightarrow 5\text{d}[7/2]_3^0$	3.6971	
	$7\text{f}[5/2]_2 \rightarrow 5\text{d}[7/2]_3^0$	3.6969	
	$7\text{f}[7/2]_{3,4} \rightarrow 5\text{d}[7/2]_3^0$	3.6920	
3.913	$4\text{d}'[3/2]_1^0 \rightarrow 5\text{p}'[1/2]_1$	3.9180	H
3.925	$5\text{p}[3/2]_2 \rightarrow 3\text{d}'[5/2]_2^0$	3.9330	
	$5\text{d}'[3/2]_1^0 \rightarrow 6\text{p}[3/2]_2$	3.9296	
	$6\text{p}[5/2]_2 \rightarrow 4\text{d}[1/2]_1^0$	3.9363	

Table 1. Tentatively Identified Spectral Transitions for Argon
Between 1.95 and 16.0 μm (Contd)

Observed Peak Wavelength (μm)	Transition	Predicted Wavelength (μm)
3.961	$7\text{f}[3/2]_2 \rightarrow 5\text{d}[5/2]_3$	3.956
	$8\text{d}[7/2]_4 \rightarrow 5\text{f}[9/2]_{4,5}$	3.962
	$8\text{d}[7/2]_1 \rightarrow 6\text{p}'[3/2]_1$	3.959
	$9\text{p}[1/2]_1 \rightarrow 5\text{d}[3/2]_1$	3.960
	$9\text{p}[1/2]_2 \rightarrow 5\text{d}[3/2]_1$	3.928
4.005	$6\text{s}[3/2]_2^0 \rightarrow 5\text{p}[3/2]_2$	3.9972
	$6\text{d}'[3/2]_1^0 \rightarrow 6\text{p}'[1/2]_0$	4.0069
	$6\text{s}[3/2]_2^0 \rightarrow 5\text{p}[3/2]_2$	4.0001
	$7\text{p}'[3/2]_2 \rightarrow 5\text{d}[7/2]_3^0$	4.0027
4.116	$6\text{d}'[3/2]_2^0 \rightarrow 6\text{p}[3/2]_2$	4.1129
4.278	$6\text{d}[3/2]_1^0 \rightarrow 6\text{p}[1/2]_0$	4.2766
4.297	$5\text{d}[3/2]_1^0 \rightarrow 4\text{f}[3/2]_2$	4.2999
	$5\text{d}[3/2]_1^0 \rightarrow 4\text{f}[3/2]_1$	4.2993
4.370	$7\text{p}[1/2]_0 \rightarrow 6\text{s}'[1/2]_0^0$	4.3698
	$5\text{d}'[5/2]_3^0 \rightarrow 6\text{p}[3/2]_1$	4.3730
	$6\text{s}'[1/2]_1 \rightarrow 5\text{p}'[1/2]_0$	4.3661
	$8\text{p}[1/2]_1 \rightarrow 5\text{d}[3/2]_2^0$	4.3680

Table 1. Tentatively Identified Spectral Transitions for Argon
Between 1.95 and 16.0 μm (Contd)

Observed Peak Wavelength (μm)	Transition	Predicted Wavelength (μm)
4.378	$4\text{d}'[5/2]_3^0 \rightarrow 5\text{p}[3/2]_2$	4.3775
	$4\text{d}[3/2]_1^0 \rightarrow 5\text{p}[1/2]_0$	4.3768
	$5\text{d}[3/2]_1^0 \rightarrow 4\text{f}[5/2]_2$	4.3779
	$6\text{p}[5/2]_2 \rightarrow 4\text{d}[5/2]_2^0$	4.3759
4.440	$5\text{d}'[5/2]_2^0 \rightarrow 6\text{p}[3/2]_1$	4.4478
	$6\text{d}[1/2]_0^0 \rightarrow 6\text{p}[3/2]_1$	4.4410
4.536	$5\text{f}'[5/2]_1 \rightarrow 5\text{d}[1/2]_1^0$	4.5361
4.720	$5\text{p}[5/2]_3 \rightarrow 3\text{d}'[5/2]_3^0$	4.7151
	$5\text{f}[7/2]_3 \rightarrow 4\text{d}'[3/2]_2^0$	4.7238
	$6\text{f}[5/2]_2 \rightarrow 5\text{d}[1/2]_1^0$	4.7198
	$6\text{d}[7/2]_3^0 \rightarrow 4\text{f}'[5/2]_2$	4.7185
	$6\text{d}[7/2]_3^0 \rightarrow 4\text{f}'[5/2]_3$	4.7179
	$6\text{d}[7/2]_3^0 \rightarrow 4\text{f}'[7/2]_{3,4}$	4.7158
6.617	$8\text{d}[5/2]_2^0 \rightarrow 7\text{p}[1/2]_1$	4.7184
	$6\text{p}[3/2]_2 \rightarrow 6\text{s}[3/2]_1^0$	6.6205
	$6\text{p}'[3/2]_1 \rightarrow 6\text{s}[1/2]_0^0$	6.6090
10.050	$7\text{d}'[3/2]_1^0 \rightarrow 7\text{p}[1/2]_1$	6.6188
	$4\text{f}[9/2]_4 \rightarrow 4\text{d}[7/2]_3^0$	10.052
	$5\text{d}[7/2]_3^0 \rightarrow 6\text{p}[5/2]_3$	10.052
10.330	$5\text{d}[7/2]_3^0 \rightarrow 6\text{p}[5/2]_2$	10.327

Table 1. Tentatively Identified Spectral Transitions for Argon
Between 1.95 and 16.0 μm (Contd)

Observed Peak Wavelength (μm)	Transition	Predicted Wavelength (μm)
10.840	$5\text{d}'[5/2]_3^0 \rightarrow 6\text{p}'[3/2]_2$	10.842
11.115	$4\text{f}'[7/2]_{3,4} \rightarrow 4\text{d}'[5/2]_3^0$	11.113
	$4\text{f}'[5/2]_3 \rightarrow 4\text{d}'[5/2]_3^0$	11.0889
11.480	$5\text{d}'[5/2]_2^0 \rightarrow 6\text{p}'[3/2]_2$	11.498
	$5\text{d}[7/2]_4^0 \rightarrow 6\text{p}[5/2]_3$	11.484
12.010	$6\text{d}[1/2]_1^0 \rightarrow 6\text{p}'[3/2]_2$	12.006
12.130	$8\text{d}[1/2]_1^0 \rightarrow 8\text{p}[1/2]_1$	12.133
12.182	$13\text{f}[3/2]_{1,2} \rightarrow 9\text{d}[3/2]_2^0$	12.182
	$18\text{s}[3/2]_1^0 \rightarrow 11\text{p}[3/2]_2$	12.186
	$9\text{s}'[1/2]_1^0 \rightarrow 8\text{f}[5/2]_2$	12.189
12.229	$11\text{d}[3/2]_1^0 \rightarrow 8\text{f}[3/2]_{1,2}$	12.230
12.255	$5\text{d}[3/2]_2^0 \rightarrow 6\text{p}[3/2]_2$	12.251
12.318	$9\text{d}[5/2]_3^0 \rightarrow 7\text{f}[7/2]_{3,4}$	12.319
12.352	$12\text{d}[1/2]_1^0 \rightarrow 6\text{f}'[5/2]_3$	12.355
	$12\text{p}[5/2]_{2,3} \rightarrow 8\text{d}[7/2]_3^0$	12.348
12.378	$10\text{p}[5/2]_2 \rightarrow 7\text{d}[5/2]_3^0$	12.376
12.385	$12\text{d}[5/2]_2^0 \rightarrow 10\text{p}[1/2]_1$	12.382
	$13\text{f}[5/2]_{2,3} \rightarrow 9\text{d}[7/2]_3^0$	12.388
	$16\text{d}[1/2]_1^0 \rightarrow 11\text{p}[1/2]_1$	12.389
12.427	$10\text{p}[5/2]_3 \rightarrow 7\text{d}[5/2]_3^0$	12.426

Table 1. Tentatively Identified Spectral Transitions for Argon Between 1.95 and 16.0 μm (Contd)

Observed Peak Wavelength (μm)	Transition	Predicted Wavelength (μm)
13.060	$5f'[5/2]_3 \rightarrow 5d'[3/2]_2^0$	13.084
	$5f'[5/2]_2 \rightarrow 5d'[3/2]_2^0$	13.081
	$7p[5/2]_3 \rightarrow 7s[3/2]_2^0$	13.060
13.271	$5f[3/2]_1 \rightarrow 5d[1/2]_1^0$	13.275
	$5f[3/2]_2 \rightarrow 5d[1/2]_1^0$	13.272
13.500	$5d[1/2]_1^0 \rightarrow 6p[5/2]_2$	13.495
	$7p[3/2]_1 \rightarrow 5d[3/2]_1^0$	13.500
13.665	$7p[1/2]_1 \rightarrow 7s[3/2]_2^0$	13.662
14.625	$4f[7/2]_{3,4} \rightarrow 4d[5/2]_3^0$	14.619
	$8s'[1/2]_0^0 \rightarrow 7p[1/2]_1$	14.626
15.570	$8p'[3/2]_2 \rightarrow 6d'[5/2]_3^0$	15.578
	$8s[3/2]_2^0 \rightarrow 7p[3/2]_2^0$	15.584
	$7d[5/2]_2^0 \rightarrow 6f[7/2]_3$	15.611

The gA factors for all selection rule allowed transitions in the $\lambda = 2$ - to 16- μm wavelength range have been computed for initial states of $n = 4, 5, 6, 7, 8, 10, 12, 14, 16, 18, 20$, and 22. The results of these calculations are presented in Figures 14 to 25, where for each value of n , gA factors are plotted vs transition wavelength. The gA values are normalized to the largest values (for each value of n) within the 2 to 16 μm range. The maximum value of gA is noted on each figure. Also noted on the right-hand vertical axis are values of $(gA)^{-1}$, proportional to the predicted lifetime of a given transition.

Several general trends in the values of gA are readily seen. Values of gA tend to decrease as the transition wavelength increases. This behavior is

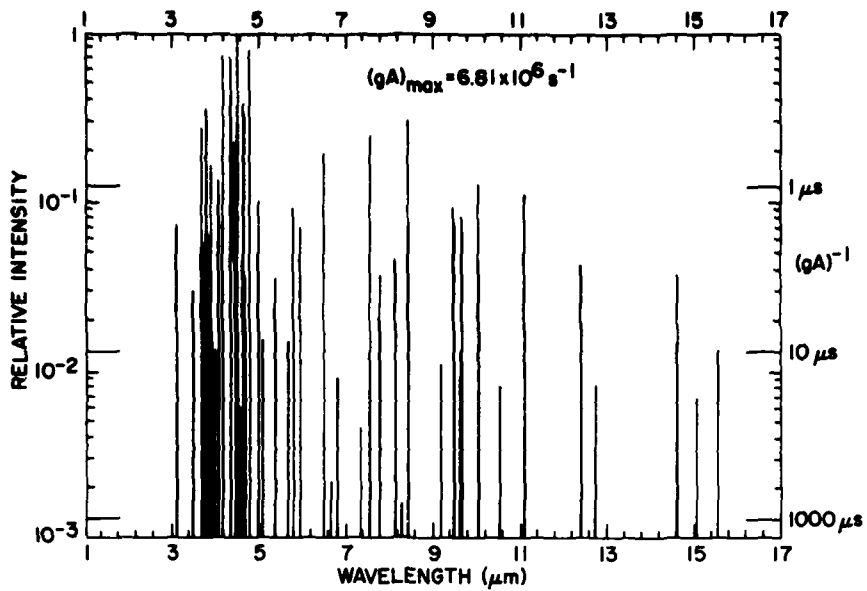


Figure 14. Computed Values of gA as a Function of Transition Wavelength (2 to 16 μm) for Argon Excited States, $[1s^2 2s^2 2p^6 3s^2 3p^5] nl, n=4$. Plotted values are normalized to the maximum value of gA , $(gA)_{\text{max}}$, noted on figure

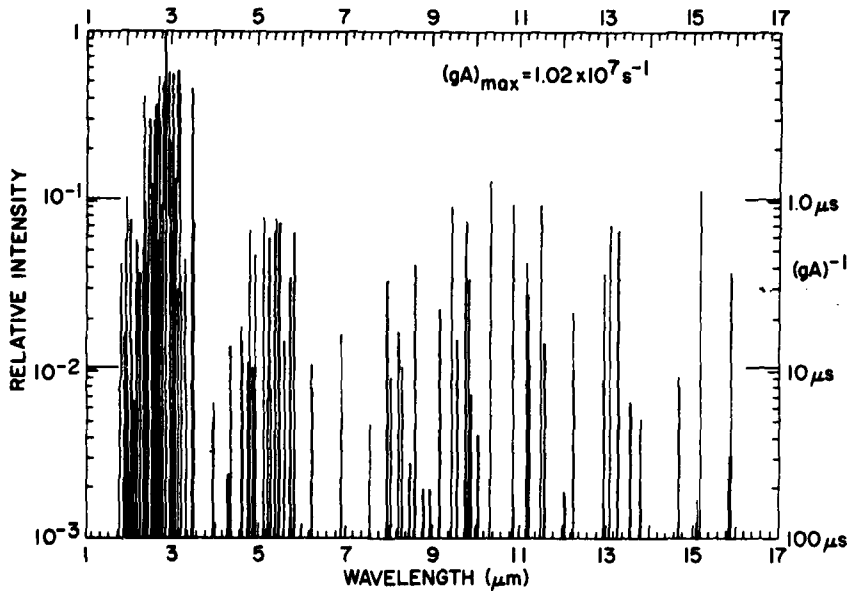


Figure 15. Computed Values of gA as a Function of Transition Wavelength (2 to 16 μm) for Argon Excited States, $[1s^2 2s^2 2p^6 3s^2 3p^5] nl, n=5$. Plotted values are normalized to the maximum value of gA , $(gA)_{\text{max}}$, noted on figure

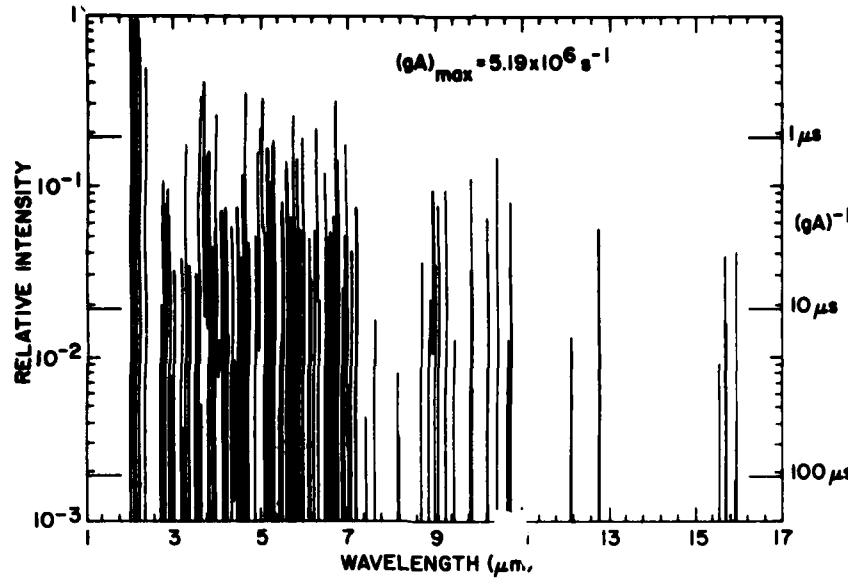


Figure 16. Computed Values of gA as a Function of Transition Wavelength (2 to 16 μm) for Argon Excited States, $[1s^2 2s^2 2p^6 3s^2 3p^5] nl, n=6$. Plotted values are normalized to the maximum value of gA , $(gA)_{\text{max}}$, noted on figure

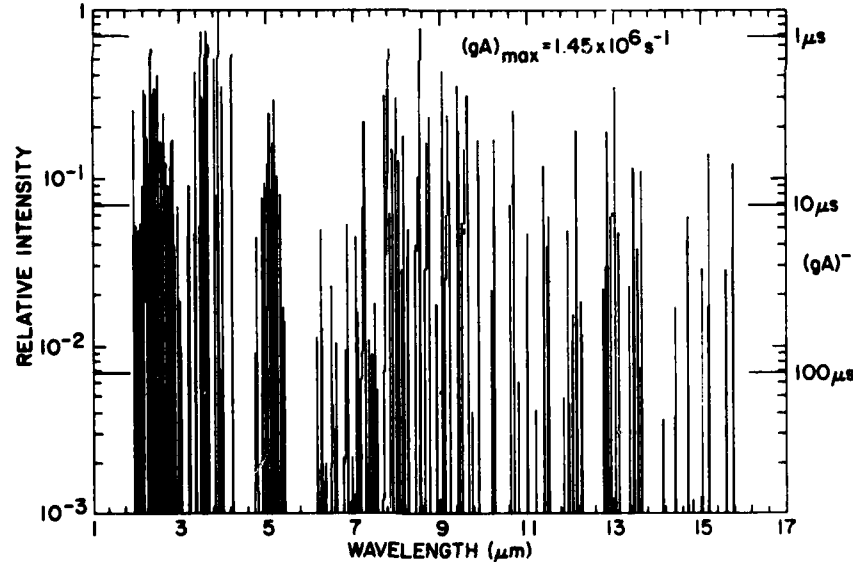


Figure 17. Computed Values of gA as a Function of Transition Wavelength (2 to 16 μm) for Argon Excited States, $[1s^2 2s^2 2p^6 3s^2 3p^5] nl, n=7$. Plotted values are normalized to the maximum value of gA , $(gA)_{\text{max}}$, noted on figure

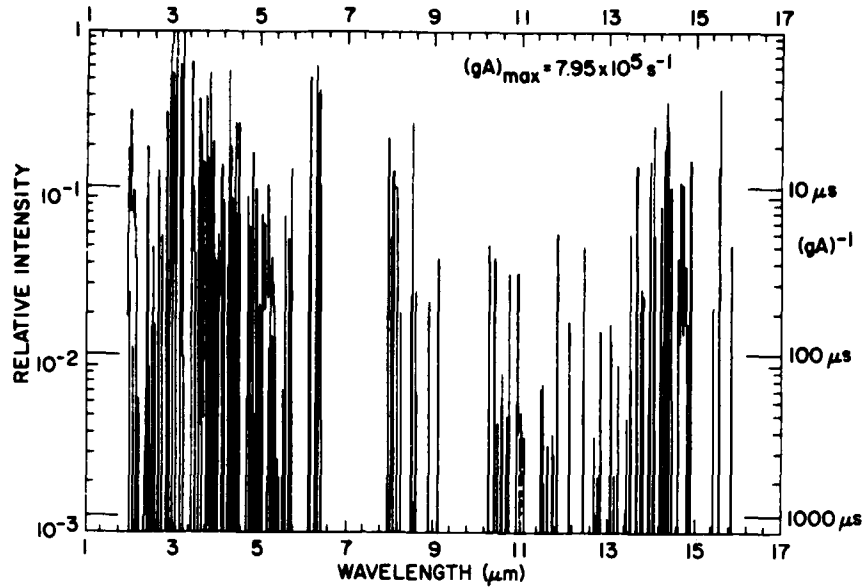


Figure 18. Computed Values of gA as a Function of Transition Wavelength (2 to 16 μm) for Argon Excited States, $[1s^2 2s^2 2p^6 3s^2 3p^5] nl$, $n=8$. Plotted values are normalized to the maximum value of gA, $(gA)_{\text{max}}$, noted on figure

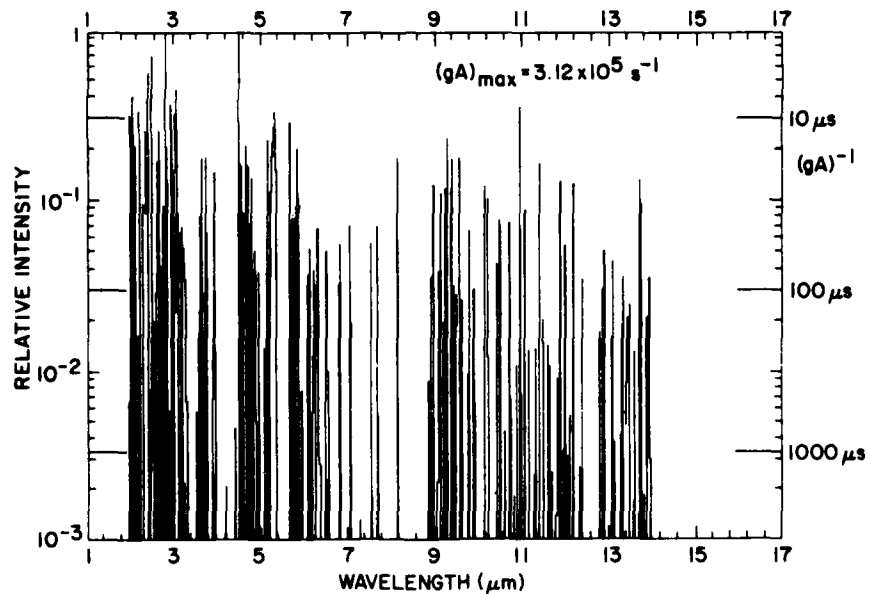


Figure 19. Computed Values of gA as a Function of Transition Wavelength (2 to 16 μm) for Argon Excited States, $[1s^2 2s^2 2p^6 3s^2 3p^5] nl$, $n=10$. Plotted values are normalized to the maximum value of gA, $(gA)_{\text{max}}$, noted on figure

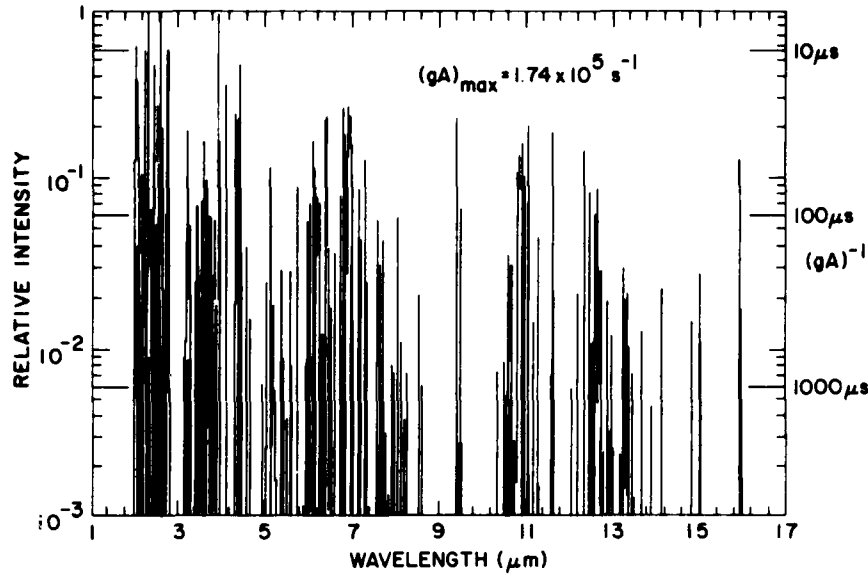


Figure 20. Computed Values of gA as a Function of Transition Wavelength (2 to 16 μm) for Argon Excited States, $[1s^2 2s^2 2p^6 3s^2 3p^5] nl$, $n=12$. Plotted values are normalized to the maximum value of gA, $(gA)_{\max}$, noted on figure

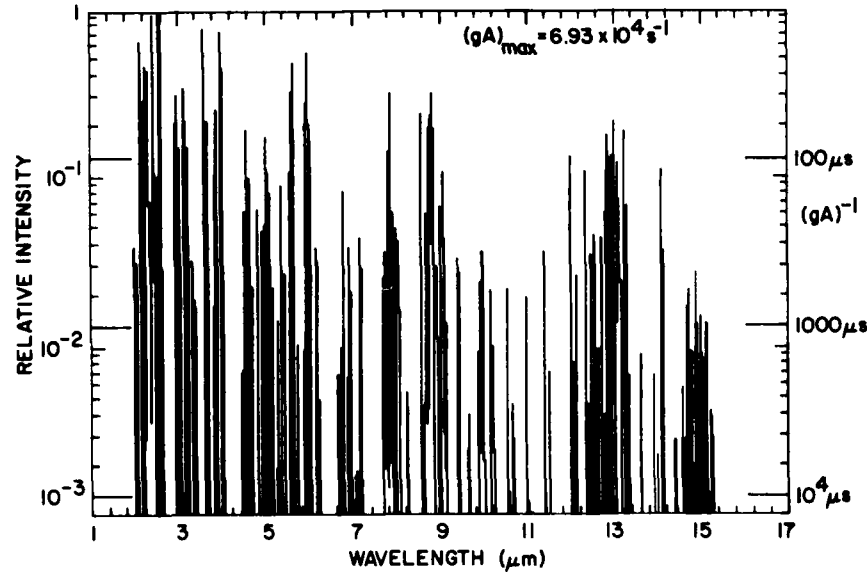


Figure 21. Computed Values of gA as a Function of Transition Wavelength (2 to 16 μm) for Argon Excited States, $[1s^2 2s^2 2p^6 3s^2 3p^5] nl$, $n=14$. Plotted values are normalized to the maximum value of gA, $(gA)_{\max}$, noted on figure

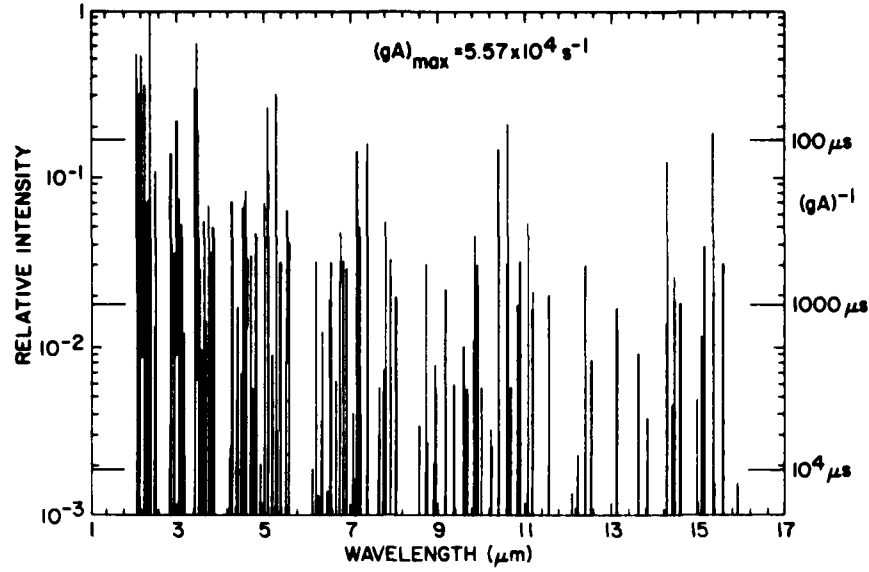


Figure 22. Computed Values of gA as a Function of Transition Wavelength (2 to 16 μm) for Argon Excited States, $[1s^2 2s^2 2p^6 3s^2 3p^5] nl$, $n=16$. Plotted values are normalized to the maximum value of gA , $(gA)_{\text{max}}$, noted on figure

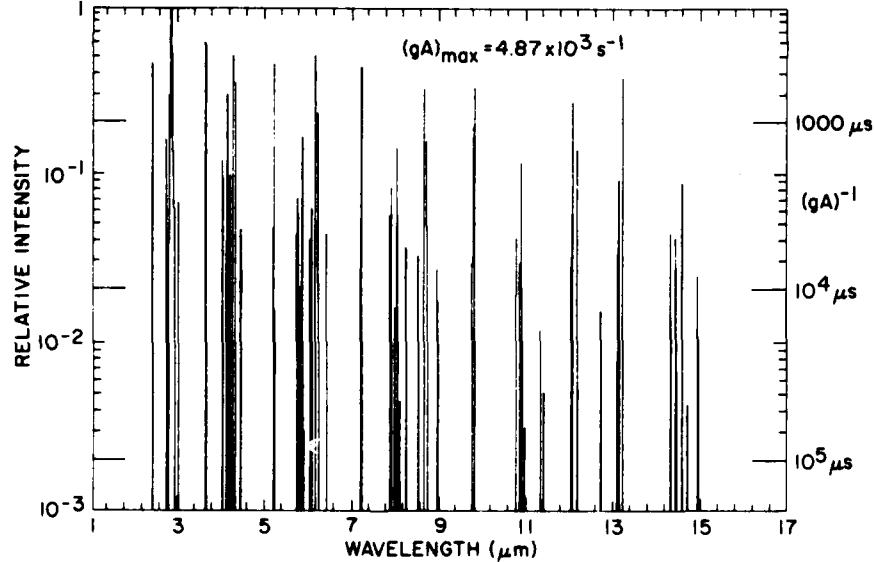


Figure 23. Computed Values of gA as a Function of Transition Wavelength (2 to 16 μm) for Argon Excited States, $[1s^2 2s^2 2p^6 3s^2 3p^5] nl$, $n=18$. Plotted values are normalized to the maximum value of gA , $(gA)_{\text{max}}$, noted on figure

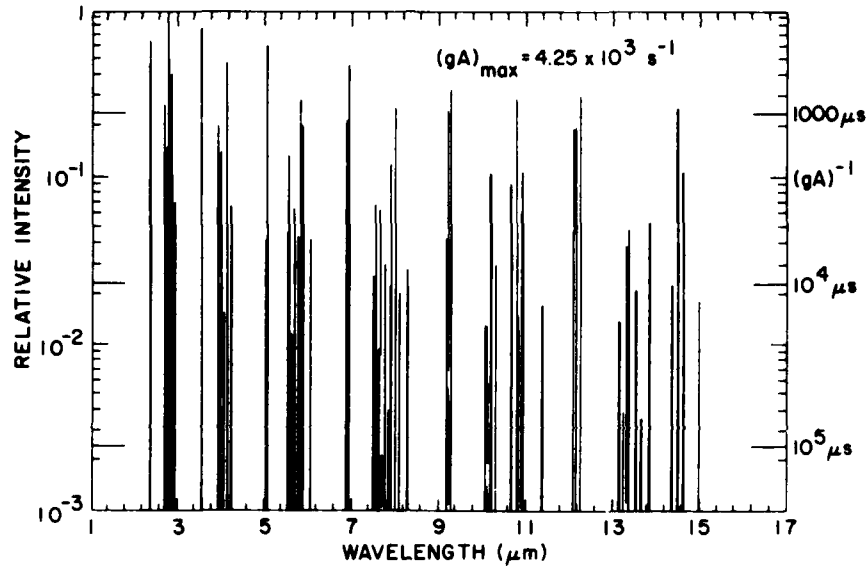


Figure 24. Computed Values of gA as a Function of Transition Wavelength (2 to 16 μm) for Argon Excited States, $[1s^2 2s^2 2p^6 3s^2 3p^5] nl$, $n=20$. Plotted values are normalized to the maximum value of gA , $(gA)_{\text{max}}$, noted on figure

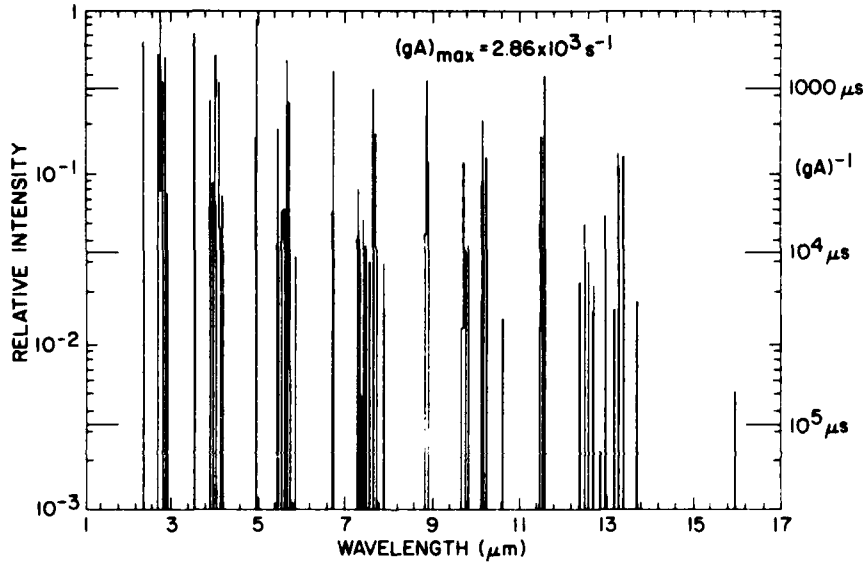


Figure 25. Computed Values of gA as a Function of Transition Wavelength (2 to 16 μm) for Argon Excited States, $[1s^2 2s^2 2p^6 3s^2 3p^5] nl$, $n=22$. Plotted values are normalized to the maximum value of gA , $(gA)_{\text{max}}$, noted on figure

dominated by the λ^{-3} factor in Eq. (11). Values of gA decrease with increasing values of principal quantum number, n . An exception to this rule is the behavior of $n = 4$ and $n = 5$, where the value of $(gA)_{\max}$ for $n = 5$ exceeds that for $n = 4$.

The largest values of gA , $(gA)_{\max}$, vary over more than 3 orders of magnitude. For values of n less than or equal to 6 there are many lines with sub-microsecond values of $(gA)^{-1}$. However, for $n \geq 10$ the strongest lines are in the several microsecond lifetime regime. Note that these time scales apply to the shorter wavelengths, 2 to 4 μm . In the 8 to 16 μm range, lifetimes are much longer. In that range, there are very few submicrosecond values of $(gA)^{-1}$ and only for $n \leq 7$. For $n \geq 10$ there are no allowed transitions with lifetimes less than 10 μs and for $n \geq 14$ (essentially) none with lifetimes less than 100 μs . Consequently, in the relatively high density environment of the COCHISE apparatus, excited states with high quantum values of n , if formed, may not be observed (between 8 and 16 μm) due to more rapid gas phase or wall quenching processes. This point will be discussed in a later section.

These calculations were made within the framework of the Coulomb approximation, usually taken to be order of magnitude in accuracy. There is evidence that we may have some confidence in the general accuracy of these calculations for specific transitions in Ar. Recently, Borge and Campos¹⁹ have measured lifetimes for several $\text{ns}[3/2]_2^0$ ($n = 6, 7, 8, 9$) states and compared their results to computed Coulomb approximation lifetimes and the results of more accurate calculations. Their comparisons indicate agreement between the Coulomb approximation predictions and measured values are within a factor of 2 for these limited transitions. For other transitions, we have found the agreement to be very unsatisfactory.

Calculations were performed to simulate Ar spectra for 8 to 16 μm as observed in COCHISE. To simulate the observed spectra, a distribution of populations of states must be chosen. We have chosen a Boltzmann distribution with a temperature of 10,000 K. Calculations were also performed at temperatures of 20,000 and 50,000 K. They showed no significant variation, since the states of interest are at high energy and exhibit only slight relative population changes with temperature. We present only results computed at 10,000 K.

The use of a Boltzmann distribution in defining state population is convenient but not realistic. In the disturbed environment of a microwave discharge it is unlikely that equilibrium is achieved. Specific non-equilibrium effects have

19. Borge, M.J.G., and Campos, J. (1983) Lifetimes of $\text{ns}[3/2]_2$ ($n = 6, 7, 8, 9$) levels and transition probabilities of 4p - ns lines of ArI, Phys. Rev. A27:1910.

previously been observed by various workers in Ar²⁰⁻²⁴ discharges and should be expected here.

In Figure 26 are the predicted spectra from excited Ar at 10,000 K and the experimentally determined COCHISE spectra in the 8 to 16 μm range. The theoretical spectrum was computed using a triangular slit function of width 0.08 μm to simulate the resolution of the experimental spectrum. The theoretical intensity is plotted in relative units of spectral radiance. Note that the ordinate scale is linear. The energy radiated at a given wavelength is given by the formula

$$I(\lambda) = \sum g_i A_{i-j} e^{-\varepsilon_i/kT} \sigma(\lambda - \lambda_{ij}) \varepsilon_{ij} ,$$

where $g_i A_{i-j}$ is the upper-state degeneracy times the Einstein coefficient for the transition between states i and j , $e^{-\varepsilon_i/kT}$ the Boltzmann factor for the upper state, ε_{ij} the energy of the transition, and $\sigma(\lambda - \lambda_{ij})$ the triangular slit function. The sum is over all possible transitions allowed in the dipole approximation.

The comparison between theory and experiment is mixed. In the interval 8.5 to 10 μm very little radiation is measured where the calculations predict substantial emission. The calculations also do not predict the shape and relative magnitude of the large spectral feature around 12.4 μm . However, with these exceptions the theoretical predictions correlate well with the observed peak positions and, within factors of 2 to 3, with relative peak heights over the rest of the spectrum, that is, the theoretical predictions seem to agree best with experiment in the 10 to 12 μm and 12.6 to 16.0 μm ranges. There are several possible explanations. The most obvious is that the Coulomb approximation is failing in the 8.5 to 10 μm region. It is curious, however, that several of the observed transitions in the 10 to 12 μm or 12.6 to 16.0 μm region originate from similar upper states as the unobserved transitions in the 8.5 to 10 μm region.

20. Wiese, W. L. (1979) Progress in Atomic Spectroscopy, Part B, W. Haule and H. Deinpoppen, Eds., Plenum Publishing Corp., New York.
21. Shiu, Y.J., and Biondi, M.A. (1978) Dissociative recombination in argon: dependence of the total rate coefficient and excited-state production on electron temperature, Phys. Rev. A 17:868.
22. Keto, J.W., and Kuo, C.Y. (1981) Cascade production of Ar(3p⁵4p) following electron bombardment, J. Chem. Phys. 74:6188.
23. Kuo, C.Y., and Keto, J.W. (1983) Dissociative recombination in electron-beam excited argon at high pressures, J. Chem. Phys. 78:1851.
24. Chang, R.S.F., and Setser, D.W. (1978) Radiative lifetimes and two-body deactivation constants for Ar(3p⁵, 4p) and Ar(3p⁵, 4p') states, J. Chem. Phys. 69:3885.

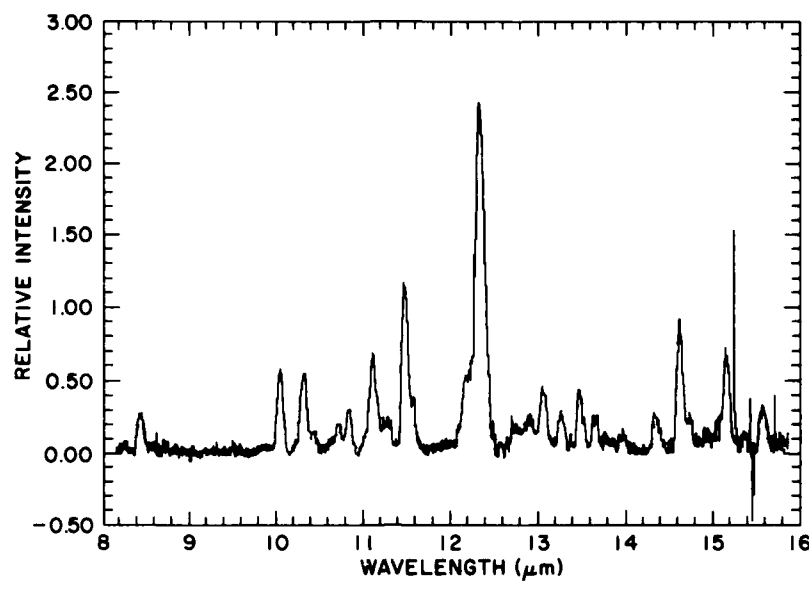


Figure 26a. Experimental COCHISE Argon Emission Spectrum, 8 to 16 μm

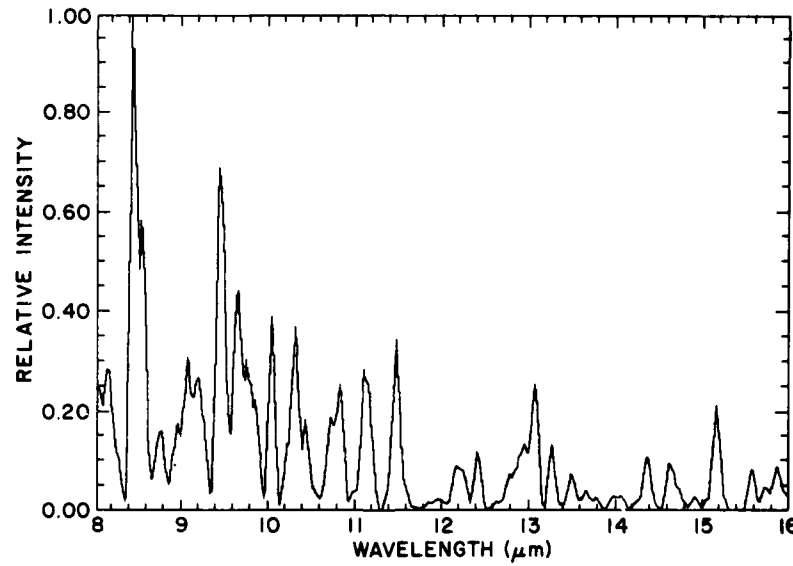


Figure 26b. Simulated Argon Spectrum, 8 to 16 μm

This may indicate that there is a non-equilibrium population due to selective excitation or cascade processes in the radiating gas.

Identified transitions in the 10 to 12 μm and 12.6 to 16.0 μm regions are listed in Table 1. Several features are noteworthy. None of the identified transitions involve core changing transitions. This is quite unlike the identified transitions at shorter wavelengths, where several strong core changing transitions are noted. There is also a tendency to see transitions from relatively high excited states. Transitions from $n = 5$ are most common with some potential transitions from $n = 8$ noted. Transitions from higher states are not needed to account for these observed spectra. It may be that higher states are not produced or that, when formed, they are quenched. A discussion of these possibilities is given in a later section on the excitation mechanisms and kinetics.

The strongest predicted transitions in the 8.5 to 10.0 μm region are listed in Table 2. The upper states of these transitions are reasonably similar to identified transitions noted in Table 1. We have examined this group to see if transitions arising from the same upper state appear in other portions of the spectrum. Most do not appear as singly identified transitions, but several appear identified with other transitions that may well cause the observed feature. Only transitions from the $4f'[7/2]_3$, $4f'[5/2]_3$, and $5d[3/2]_2$ states seem to be definitely identified at 11.115, 11.115, and 12.255 μm , respectively.

For the strong transitions predicted between 8.5 to 10 μm , we might speculate that, for states not radiating elsewhere in the observed spectrum, non-equilibrium effects from selective excitation or cascade may cause them not to be populated. The seemingly missing predicted radiation from 4f states between 9.497 and 9.671 μm might well be due to the breakdown of the Coulomb approximation for 4f states. The Coulomb approximation limits are generally accepted to be $n - l \geq 1$, so that this case is at best borderline. The possibility of non-equilibrium populations is quite intriguing although we readily admit to the quantitative limitations of the Coulomb approximation.

The predicted and experimentally measured spectra for Ar radiation between 11.90 and 12.50 μm are shown in Figure 27. The theoretical spectrum was computed using a triangular slit function of width 0.013 μm to simulate the resolution of the experimental spectrum. The theoretical spectrum is again plotted in relative units of power radiated/wavelength. Comparison between the theoretical and experimental spectra is nominal. Most of the peaks in the measured spectrum are accounted for except for those around 12.35 to 12.40 μm . Identified lines in this spectral region are listed in Table 1. Note that no particularly strong lines are predicted at 12.352 and 12.385 μm . The origin of these intense lines is not apparent. However, the observed features between 12 and 12.5 μm

Table 2. Spectral Transitions: 8.50 to 10.00 μm

Transition	Predicted Wavelength (μm)
$4f'[7/2]_3 \rightarrow 4d'[5/2]_2^0$	9.668
$4f'[5/2]_3 \rightarrow 4d'[3/2]_2^0$	9.493
$5d[3/2]_2^0 \rightarrow 6p[3/2]_1$	9.822
$5d[5/2]_2^0 \rightarrow 6p[1/2]_1$	9.757
$5d'[3/2]_1^0 \rightarrow 6p'[1/2]_0$	9.757
$5d[3/2]_1^0 \rightarrow 6p[1/2]_0$	9.579
$5d[5/2]_3^0 \rightarrow 6p[3/2]_2$	9.443
$5d[5/2]_2^0 \rightarrow 6p[5/2]_2$	9.172
$5d[5/2]_3^0 \rightarrow 6p[5/2]_3$	8.589
$6d'[5/2]_3^0 \rightarrow 5f[7/2]_4$	9.859
$6d[7/2]_3^0 \rightarrow 5f[9/2]_4$	9.275
$6d[5/2]_2^0 \rightarrow 5f[7/2]_3$	9.018
$7f'[5/2]_2 \rightarrow 6d'[3/2]_1^0$	9.913
$7f[7/2]_4 \rightarrow 6d[5/2]_3^0$	9.650
$4p[5/2]_2 \rightarrow 5d[7/2]_3^0$	9.429
$7p'[5/2]_1 \rightarrow 5d'[5/2]_2^0$	8.787
$7s[3/2]_2^0 \rightarrow 6p[3/2]_2$	8.551
$7p[5/2]_3 \rightarrow 5d[7/2]_4^0$	8.548

can be accounted for by invoking transitions from extremely high levels, $n \geq 9$. The difficulty here is that, because of the relatively long radiative lifetimes for such transitions, large steady-state populations of these levels are required to explain the intense emission we observe. This point will be explored further in Section 5.

In summary, the theoretical spectra (computed in the Coulomb approximation) give variable agreement with the LWIR COCHISE (8 to 16 μm) spectra. Several significant discrepancies exist, and specifically the theory fails to predict the relatively strong radiation at around 12.40 μm .

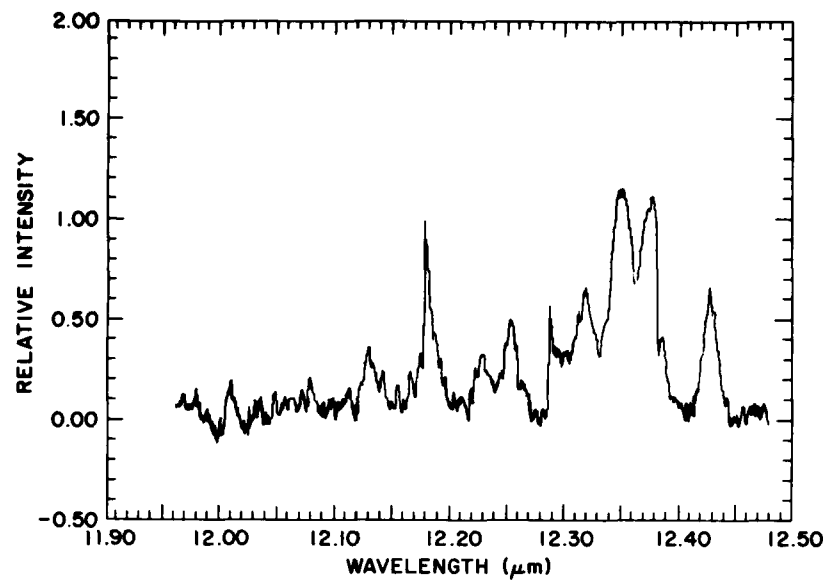


Figure 27a. Experimental COCHISE Argon Emission Spectrum, 11.90 to 12.50 μm

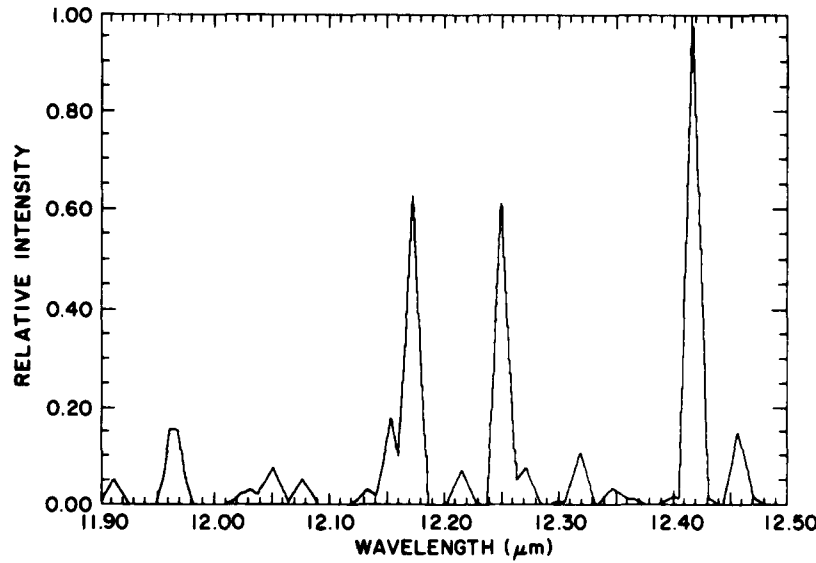


Figure 27b. Simulated Argon Spectrum, 11.90 to 12.50 μm

5. DISCUSSION

5.1 Kinetic Interpretations

Careful inspection of the transitions listed in Table 1 leads to several interesting observations. For convenience, the observed manifold-to-manifold transitions are depicted in Figures 28 to 30.

First, emission is observed from states up to within a few hundred cm^{-1} of the ionization limit for the $j_c = 3/2$ (unprimed) core configuration. This is far higher in the energy manifold than has been probed in other electron bombardment experiments,²¹ in which only emission in the visible was monitored.

Second, emitting states above 124,000 cm^{-1} are not uniformly represented by observable transitions. This is contrary to what we might expect for excitation solely by direct electron impact. Electron impact excitation will occur in the tail of the electron energy distribution with cross sections similar to that for ionization. This should give rise to a uniform population distribution, with the relative state populations decreasing with increasing energy. Collisional relaxation may modify this distribution somewhat, but this modification should not strongly affect the distributions under our conditions. Quenching studies²²⁻²⁴ for the 4p and 4p' manifolds yield collisional deactivation rate coefficients in the $10^{-11} \text{ cm}^3 \text{ s}^{-1}$ range, probably occurring via curve crossings on the Ar₂ potential surface.²⁴ For our conditions, 0.1 Torr, 100 K, [Ar] = 10^{16} cm^{-3} , the collisional lifetime of Ar* would be $\sim 10 \mu\text{s}$, that is, on the order of the infrared radiative lifetimes for the higher levels ($n \sim 10$). Additional rapid quenching by electronic-to-translational energy transfer may be expected for states above $n \sim 12$, where the energy defects are on the order of kT or less. Thus, we expect quenching to deplete levels above 125,000 cm^{-1} , but in a non-selective way. The implication is, then, that the few observed emitting states above 125,000 cm^{-1} , which radiate predominantly at long wavelengths, are directly populated by some rapid kinetic process. This is consistent with the results of the spectral analysis, which show that the upper-level electronic population distribution cannot be described by a Boltzmann expression, but rather exhibits a population enhancement for LWIR-radiating states. The LWIR emissions from these states, as well as their collisional deactivation, appear to be the initial steps in a (largely radiative) cascade sequence that populates the lower levels. As the cascade moves down the energy "ladder", the radiative lifetimes become shorter, quenching becomes less important, and the radiative transitions occur at shorter wavelengths. Below $\sim 122,000 \text{ cm}^{-1}$, virtually every electronic state manifold can be accounted for in the infrared spectrum. Note that the relative populations within manifolds can still be non-Boltzmann due to the selectivity of

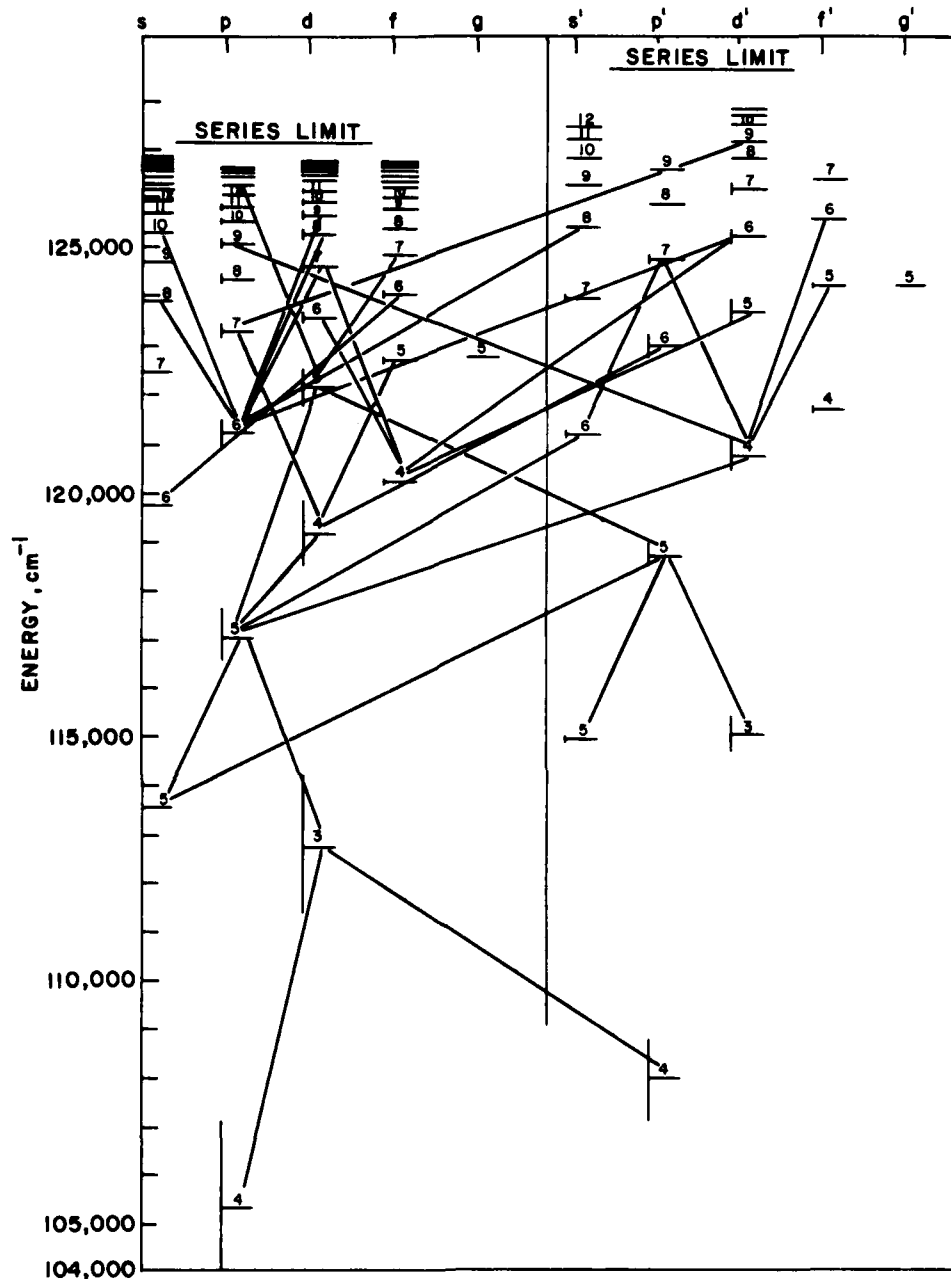


Figure 28. Observed ArI Transitions, 2 to 3.5 μ m

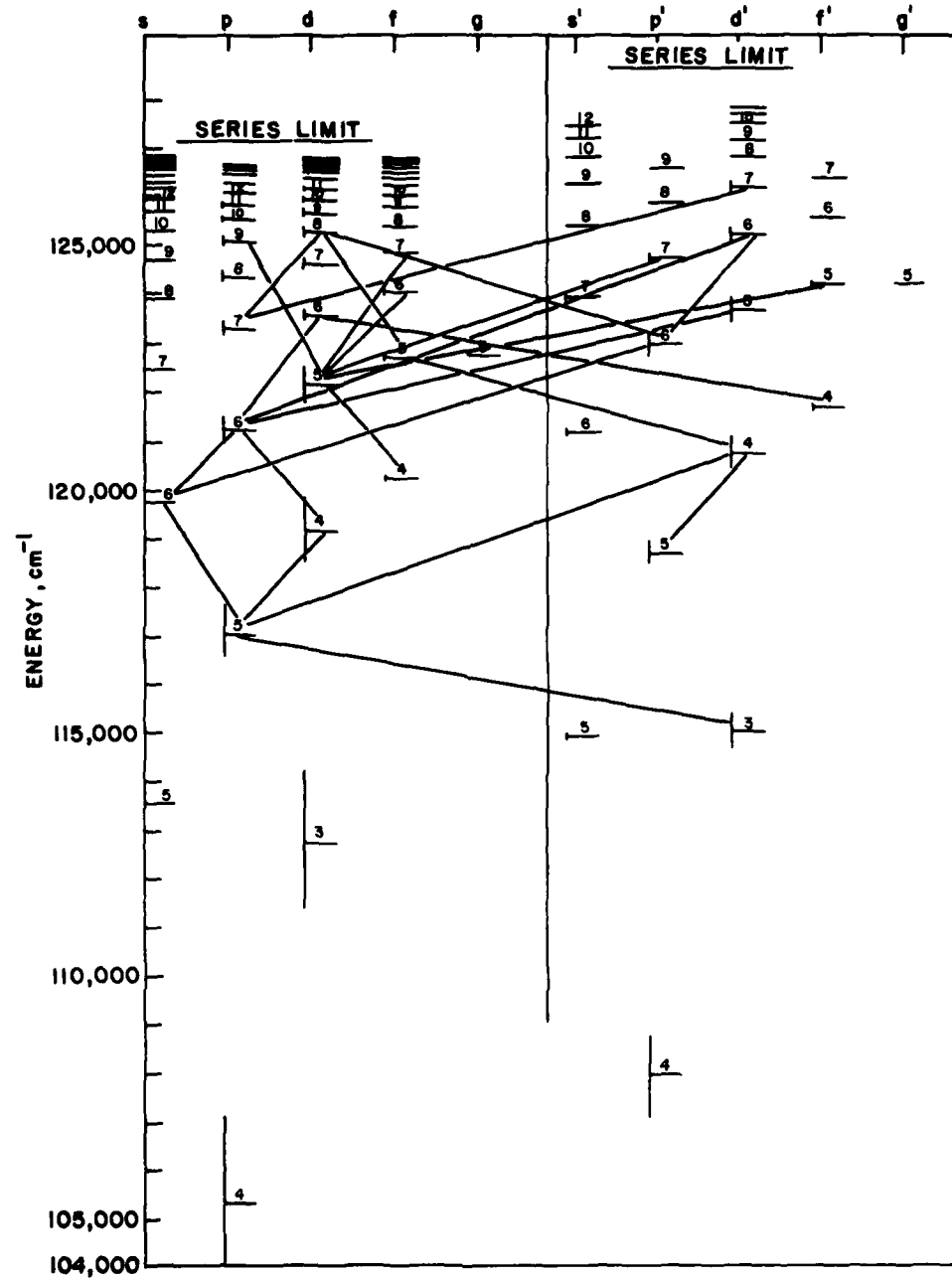


Figure 29. Observed ArI Transitions, 4 to 7 μ m

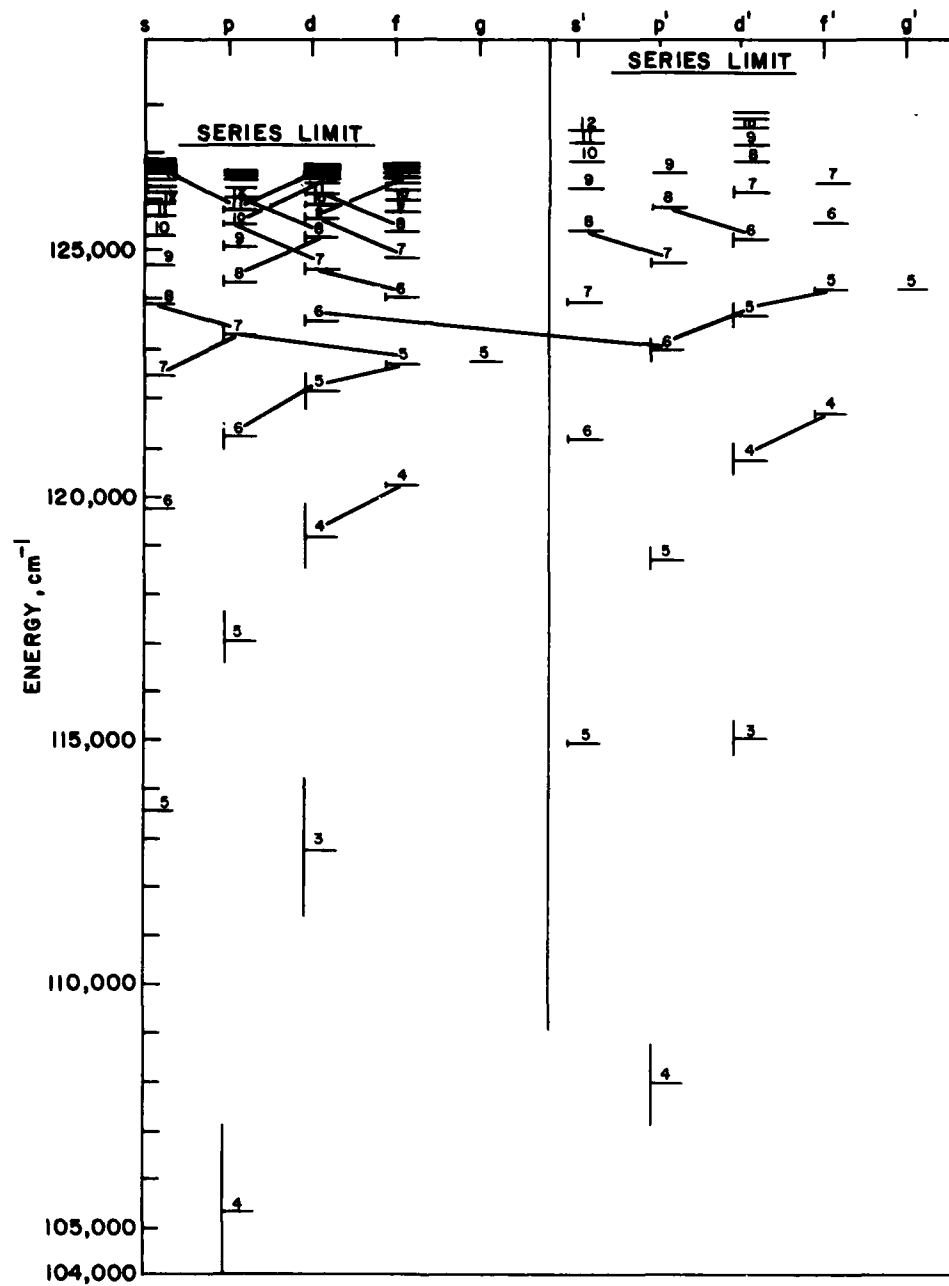


Figure 30. Observed ArI Transitions, 10 to 16 μm

the radiative transitions in and out. This effect has been observed even at high pressures.^{22,23} Such selective excitation within manifolds can explain the observed absence of certain predicted transitions, as discussed in the previous section.

Third, the observed transitions occur primarily in the $j_c = 3/2$ manifold. Of the few $j_c = 1/2$ transitions we observe, most of them occur at shorter wavelengths, and the highest states observed lie at substantially lower energies than those observed for $j_c = 3/2$. The implication here is that there is little or no direct formation of Ar* with the $j_c = 1/2$ core, and that the higher states we observe are populated initially by collisional energy transfer from Ar* ($j_c = 3/2$).

Fourth, there are some manifolds at intermediate points in the cascade for which there are several radiative inputs and few radiative outputs. This is especially true for the 6p manifold, and also to some extent for 5d, 4f, 4d, and 5p. The "bottleneck effect" in evidence for these manifolds may be expected to give unusual state distributions within each manifold and intense radiative transitions at selected wavelengths, especially in the near infrared ($\lambda < 2 \mu\text{m}$), where the strongest emissions for these states will occur.

It remains to identify the excitation process responsible for initiating the cascade. An obvious candidate is the dissociative recombination of Ar₂⁺



where Ar* is in one of many possible Rydberg states. Direct recombination of Ar⁺ with electrons in a three-body, bielectronic process and will be extremely slow in a low-pressure, weak plasma, such as occurs in our discharges. Similarly, two-body radiative dielectronic recombination of Ar⁺ will not be significant under our conditions. Reaction (12) has been carefully studied by Shiu and Biondi²¹ for electron temperatures of 300 to 7500 K. By monitoring radiation in the visible, they observed formation of Ar (4p, 4p') in the recombination of Ar₂⁺ with 300 K electrons, and formation of states as high as 5d when 7200 K electrons were used. They deduced that the observed states were populated directly from Ar₂⁺, whose zero-point energy lies near 117,000 cm⁻¹ (binding energies of 1.4, 1.23 ± 0.02, and 1.33 ± 0.02 eV are reported in References 25 to 27,

25. Mullikan, R.S. (1970) Potential curves of diatomic rare-gas molecules and their ions, with particular reference to Xe₂*. *J. Chem. Phys.* 52:5170.
26. Ng, C.Y., Trevor, D.J., Mahan, B.H., and Lee, Y.T. (1977) Photoionization studies of the Kr₂ and Ar₂ van der Waals molecules. *J. Chem. Phys.* 66:446.
27. Moseley, J.T., Saxon, R.P., Huber, B.A., Cosby, P.C., Abouaf, R., and Tadjeddine, M. (1977) Photofragment spectroscopy and potential curves of Ar₂. *J. Chem. Phys.* 67:1659.

respectively). However, since infrared emission was not monitored in their experiments, it is not clear whether the observed states were populated directly or by radiative cascade from above. In any case, Shiu and Biondi's experiments show that energetic electrons can recombine with Ar_2^+ to form Ar^* with most of the excess energy going into electronic excitation of the Ar^* . For the microwave discharge case, with an electron temperature of $2 - 3 \times 10^4$ K, one can expect population of states near the ionization limit, as we observe spectroscopically. (There may also be substantial formation of $\text{Ar}^+(^2\text{P}_{3/2})$ by this route.) Of course, we cannot eliminate the possibility that intermediate states of Ar^* are directly populated as well, which will exacerbate the non-Boltzmann character of the cascade process.

Reaction (12) can only explain our observations if there is sufficient formation of Ar_2^+ in a microwave discharge. Ar_2^+ can be formed by three-body recombination of Ar^+ :



However, Reaction (13) has a rate coefficient of the order of $10^{-31} \text{ cm}^6 \text{ s}^{-1}$ at room temperature,²⁸ giving it an effective bimolecular rate coefficient of $\sim 10^{-15} \text{ cm}^3 \text{ s}^{-1}$ at 0.1 Torr. By comparison, direct electron impact excitation of Ar^* should occur with an effective rate coefficient similar to that for ionization; Caledonia²⁹ has calculated the latter quantity to be in the range $10^{-12 \pm 1} \text{ cm}^3 \text{ s}^{-1}$ for typical microwave discharges. Thus, we anticipate that the Ar_2^+ mechanism, with Reaction (13) as a rate-limiting step, would not be able to compete with electron impact excitation as a source for Ar^* unless the pressure is considerably larger. However, as pointed out by Shiu and Biondi,²¹ the reverse of Reaction (12), associative ionization of Ar^* , is probably very facile, with a rate coefficient of at least $10^{-9} \text{ cm}^3 \text{ s}^{-1}$. Thus, it is possible to form Ar_2 from less energetic Ar^* produced in electron impact, and then recombine the Ar_2^+ with "hot" electrons to form highly energetic Ar^{**} :



-
- 28. Good, A. (1975) Third-order ion-molecule clustering reactions, Chem. Rev. 75:561.
 - 29. Caledonia, G.E. Unpublished work. See Appendix C of Rawlins, W.T., Piper, L.G., Gelb, A., Lucht, R.A., and Caledonia, G.E. (1983) COCHISE Research, PSI-TR 349, Physical Sciences Inc., Andover, Mass.



Here e^-_{hot} denotes the relatively energetic "average" electron in the plasma. Although the recombination coefficient decreases with increasing electron energy, the electron energy distribution is such that most recombinations will occur with relatively energetic electrons. Ar^{**} is then a highly excited Rydberg species with a $^2P_{3/2}$ core configuration, and is subject to collisional and radiative deactivation as outlined above, as well as to rapid electron-impact ionization. The specificity of the process for the $^2P_{3/2}$ core can be understood in terms of the adiabatic dissociation of the $Ar_2^+ - e^-$ associated pair along the $Ar - Ar^+(^2P_{3/2})e^-$ coordinate: the complex behaves like Ar_2^+ and dissociates to form the lowest-energy ionic (core) configuration of the atomic "ion".

Reactions (15) and (16) in effect set up a quasi-equilibrium between Ar_2^+ and the atomic Rydberg manifold, such that the net removal of Rydberg atoms is controlled primarily by radiative and collisional cascade. Recombination of Ar_2^+ and e^-_{cold} (the reverse of (15)) can also occur; however, this reaction only feeds back Ar^* and should not constitute a major loss term for Ar_2^+ . Since this reaction is dominated by ambient-temperature electrons, we anticipate that, in the active discharge, the principal fate of Ar_2^+ is recombination with e^-_{hot} in Reaction (16). In steady state, the Ar_2 and Ar^{**} number densities are given by:

$$[Ar_2^+] = \frac{k_a [e^-]}{k_c [e^-_{\text{hot}}]} [Ar] \quad (17)$$

$$[Ar^{**}] = \frac{k_a [e^-] [Ar]}{L} , \quad (18)$$

where L is the effective first-order loss rate of Ar^{**} by collisional and radiative deactivation and is of order 10^6 s^{-1} . We can see from Eq. (18) that $[Ar^{**}]$ depends upon the effective rate for electron-impact excitation of Ar^* . This rate is extremely sensitive to pressure through the field/density ratio E/N for the discharge; indeed, the ionization rate coefficient increases 2 orders of magnitude for a two-fold increase of E/N .²⁹ Thus, the pressure effect we observe is undoubtedly due largely to changes in discharge conditions such as E/N and $[e^-]$.

An order-of-magnitude estimate from Eq. (18) gives $[Ar^{**}] \sim 10^{10} \text{ cm}^{-3}$ in the active discharge. For a gA factor of $\sim 10^4 \text{ s}^{-1}$, this value yields a spectral radiance of $\sim 10^{-5} \text{ W cm}^{-2} \text{ sr}^{-1} \mu\text{m}^{-1}$ at $12 \mu\text{m}$. This is to be compared to the apparent value of $\sim 2 \times 10^{-9} \text{ W cm}^{-2} \text{ sr}^{-1} \mu\text{m}^{-1}$ determined in our experiments by neglecting geometric effects. Given the three-order-of-magnitude reduction in signal we expect due to multiple light scattering, the predicted and observed emission levels are consistent with each other. Clearly, direct observation of the discharge plasma in COCHISE would provide a great deal more information; however, such experiments require extensive reconfigurations, which are presently incompatible with our on-going chemiluminescence investigations. We are considering future experiments incorporating such modifications.

5.2 Upper Atmospheric Implications

Neutral Ar is a significant constituent of the thermosphere, having mixing ratios of 10^{-2} at 90 km and 10^{-3} at 140 km.² The number density of Ar is consistently about 3 or 4 orders of magnitude larger than that of O₃ in this altitude range. At the low pressures characteristic of these altitudes ($< 10^{-3}$ Torr), excitation of Ar Rydberg emission in an electron event could occur via the same general mechanism that appears to control its production in the COCHISE experiments, with an important exception: deactivation of Ar* and Ar** would be entirely radiative. This means that much of the Ar* formed initially by electron-impact would radiate rather than associatively ionize with Ar. Thus, we might expect the radiation signature to be more characteristic of direct excitation by electrons, that is, the LWIR component would be diminished. In a full limb-viewing aspect, for gA $\sim 10^4 \text{ s}^{-1}$ near $10\text{-}12 \mu\text{m}$, a typical instrumental noise level of $\sim 10^{-10} \text{ W cm}^{-2} \text{ sr}^{-1}$ would correspond to a minimum detectable emitter concentration of order 1 cm^{-3} , or a production rate of Ar* of $\sim 10^4 \text{ cm}^{-3} \text{ s}^{-1}$. Judging from predicted auroral ion-pair production rates,³⁰ this level of direct Ar* formation is not unreasonable for a strong (IBC III) aurora. However, in a normal atmospheric scenario, it is unlikely that sufficient excitation could occur to give measurable emission for zenith aspects, which require number densities 2 orders of magnitude larger. For extraordinary events such as nuclear phenomena, Ar Rydberg emission near $12 \mu\text{m}$ (and elsewhere in the LWIR) would probably be significant for any viewing geometry.

The COCHISE results for ArI may hold implications for atmospheric OI and NI emission in the LWIR. Unlike Ar₂⁺, O₂⁺ and N₂⁺ are readily formed by direct ionization of air; the recombination of these ions with energetic electrons may

30. Caledonia, G. E., and Kennealy, J. P. (1982) NO infrared radiation in the upper atmosphere, Planet. Space Sci. 30:1043.

lead to the formation of high Rydberg states of O and N. If the initially populated Rydberg states are high enough, substantial line radiation could occur in the 10- to 16- μm region in a strong aurora. However, the spectral signature is difficult to predict theoretically because of the non-Boltzmann character of the initial formation and cascade. We plan to pursue this point with laboratory experiments on low-pressure (< 1 Torr) Ar/N₂ and Ar/O₂ discharges and with spectral simulations using the methodologies we have applied to the ArI data.

6. CONCLUSIONS

We have used the COCHISE apparatus to obtain a new and unique set of spectroscopic data on infrared emission from Ar Rydberg atoms by observing scattered light from a low-pressure microwave discharge plasma. These measurements are the first laboratory observations of LWIR Rydberg emission, and exhibit a rich spectrum from 2 to 16 μm . Commonly used hydrogenic approximations often applied to other Rydberg atoms cannot account for the complex nature of this spectrum, but all the observed transitions can be identified as ArI lines or groupings using tabulated energy levels together with the strong (dipole-allowed) selection rules and, in several cases, also allowing the core configuration to change in the transition. A Coulomb approximation to the dipole moment function is only partially successful in accounting for the observed intensities of the dipole-allowed transitions, as it fails to predict detailed spectral distributions at shorter wavelengths ($\lambda < 5 \mu\text{m}$), where core-changing transitions are important. The spectral distribution in the LWIR portion of the spectrum exhibits a remarkable peak near 12 μm that can only be accounted for by a non-Boltzmann population distribution with a strong enhancement of very high states within a few hundred cm⁻¹ of the ionization limit. The most likely source of this distribution is the dissociative recombination of Ar₂⁺ with energetic electrons in the active discharge, followed by rapid collisional and radiative cascade. These infrared measurements are the first observations of such high excitation in dissociative recombination; previous workers have studied only visible emissions, which are the end results of the cascade process.

The ArI emission studied here may have some bearing on high-altitude LWIR observations, particularly near 12 μm . However, although Ar is a significant thermospheric species, it is difficult to form substantial levels of Ar₂⁺ at high altitudes, so ArI radiation is probably observable only in limb-viewing aspects of relatively strong electron disturbances. Of greater atmospheric significance are the implications of these results for ionized air, that is, that O₂⁺ and N₂⁺ may also recombine with energetic electrons to initiate an infrared cascade sequence of OI and NI Rydberg emission. We will pursue this latter issue in further laboratory experiments on the COCHISE facility.

References

1. Feneuille, S., and Jacquinot, P. (1981) Atomic Rydberg states, Adv. Atomic Molec. Phys. 17:99.
2. Jacchia, L.G. (1977) Thermospheric Temperature, Density, and Composition: New Models, Smithsonian Astrophysical Observatory Special Report 375.
3. Rawlins, W.T., Caledonia, G.E., and Kennealy, J.P. (1981) Observation of spectrally resolved infrared chemiluminescence from vibrationally excited O₃(v₃), J. Geophys. Res. 86:5247.
4. Rawlins, W.T., Piper, L.G., Green, B.D., Wilemski, G., Goela, J.S., and Caledonia, G.E. (1980) LABCEDE and COCHISE Analysis II, Vol. I (Final Report) PSI-TR 207A, Physical Sciences Inc., Andover, Mass.
5. Rawlins, W.T., Piper, L.G., Caledonia, G.E., and Green, B.D. (1981) COCHISE Research, PSI-TR 298, Physical Sciences Inc., Andover, Mass.
6. Rawlins, W.T., Murphy, H.C., Taylor, R.L., and Caledonia, G.E. (1980) Final Report on COCHISE Refurbishment, PSI-TR 222, Physical Sciences Inc., Andover, Mass.
7. Kennealy, J.P., DelGreco, F.P., Caledonia, G.E., and Rawlins, W.T. (1979) COCHISE: Laboratory spectroscopic studies of atmospheric phenomena with high-sensitivity cryogenic instrumentation, G.A. Vanesse, Ed., Proc. Soc. Photo-Opt. Instrum. Eng. 191:151.
8. Kennealy, J.P., DelGreco, F.P., Caledonia, G.E., and Green, B.D. (1978) Nitric oxide chemiexcitation occurring in the reaction between metastable nitrogen atoms and oxygen molecules, J. Chem. Phys. 69:1574.
9. Caledonia, G.E., Green, B.D., Simons, G.A., Kennealy, J.P., Robert, F.X., Corman, A., and DelGreco, F.P. (1977) COCHISE Studies I: Fluid Dynamical and Infrared Spectral Analyses, AFGL-TR-77-0281, AD A053218.
10. Rawlins, W.T., and Armstrong, R.A. (1982) COCHISE Observations of O₃ Formed by Three-Body Recombination of O and O₂, AFGL-TR-82-0273, AD A123653.

11. Kaufman, F. (1969) The production of atoms and simple radicals in glow discharges, Adv. Chem. Ser. 80:29.
12. Moore, C. E. (1971) Atomic Energy Levels, Vol. 1, NSRDS-NBS35.
13. Bashkin, S., and Stoner, J. O., Jr. (1978) Atomic Energy - Level and Grotrian Diagrams 2, North-Holland Publishing Co., New York.
14. Bates, D. R., and Damgaard, A. (1949) The calculation of the absolute strengths of spectral lines, Phil. Trans. Roy. Soc. A242:101.
15. Statz, H., Tang, C. L., and Koster, G. F. (1963) Approximate electromagnetic transition probabilities and relative electron excitation cross sections for rare-gas masers, J. Appl. Phys. 34:2625.
16. Koster, G. F., and Statz, H. (1964) Probabilities for the neon laser transitions, J. Appl. Phys. 35:2654.
17. Friedrich, H., Katterbach, K., and Trefftz, E. (1970) On the accuracy of machine programs for calculating oscillator strengths by Coulomb approximation, J. Quant. Spectrosc. Radiat. Trans. 10:11.
18. Humphreys, C. J. (1974) First spectra of neon, argon and xenon 136 in the 1.2-4.0 μm region, J. Phys. Chem. Ref. Data 2:519.
19. Borge, M. J. G., and Campos, J. (1983) Lifetimes of $\text{ns}[3/2]_2$ ($n = 6, 7, 8, 9$) levels and transition probabilities of 4p - ns lines of ArI, Phys. Rev. A 27:1910.
20. Wiese, W. L. (1979) Progress in Atomic Spectroscopy, Part B, W. Haule and H. Deinpoppen, Eds., Plenum Publishing Corp., New York.
21. Shiu, Y. J., and Biondi, M. A. (1978) Dissociative recombination in argon: dependence of the total rate coefficient and excited-state production on electron temperature, Phys. Rev. A 17:868.
22. Keto, J. W., and Kuo, C. Y. (1981) Cascade production of $\text{Ar}(3p^54p)$ following electron bombardment, J. Chem. Phys. 74:6188.
23. Kuo, C. Y., and Keto, J. W. (1983) Dissociative recombination in electron-beam excited argon at high pressures, J. Chem. Phys. 78:1851.
24. Chang, R. S. F., and Setser, D. W. (1978) Radiative lifetimes and two-body deactivation constants for $\text{Ar}(3p^5, 4p)$ and $\text{Ar}(3p^5, 4p')$ states, J. Chem. Phys. 69:3885.
25. Mullikan, R. S. (1970) Potential curves of diatomic rare-gas molecules and their ions, with particular reference to Xe_2^* , J. Chem. Phys. 52:5170.
26. Ng, C. Y., Trevor, D. J., Mahan, B. H., and Lee, Y. T. (1977) Photoionization studies of the Kr_2 and Ar_2 van der Waals molecules, J. Chem. Phys. 66:446.
27. Moseley, J. T., Saxon, R. P., Huber, B. A., Cosby, P. C., Abouaf, R., and Tadjeddine, M. (1977) Photofragment spectroscopy and potential curves of Ar_2^+ , J. Chem. Phys. 67:1659.
28. Good, A. (1975) Third-order ion-molecule clustering reactions, Chem. Rev. 75:561.
29. Caledonia, G. E. Unpublished work. See Appendix C of Rawlins, W. T., Piper, L. G., Gelb, A., Lucht, R. A., and Caledonia, G. E. (1983) COCHISE Research, PSI-TR 349, Physical Sciences Inc., Andover, Mass.
30. Caledonia, G. E., and Kennealy, J. P. (1982) NO infrared radiation in the upper atmosphere, Planet. Space Sci. 30:1043.

Distribution List

Director	Air Force Geophysics Laboratory
Defense Nuclear Agency	Hanscom AFB, MA 01731
Washington, DC 20305	
ATTN: RAAE W. McKechney	ATTN: CV Col D'Arcy (1 cy)
ATTN: TITL	ATTN: LKB J. Paulson (1 cy)
ATTN: RAAE H. Fitz, Jr.	ATTN: OPR-1 (1 cy)
ATTN: RAAE P. Lunn	ATTN: SULL (1 cy)
ATTN: RAEE P. Crowley	ATTN: LKB E. Murad (1 cy)
	ATTN: LKD C. Philbrick (1 cy)
	ATTN: LKB K. Champion (1 cy)
	ATTN: LKB T. Keneshea (1 cy)
Superintendent	ATTN: LKB W. Swider, Jr (1 cy)
Naval Postgraduate School	ATTN: LKO R. Huffman (1 cy)
Monterey, CA 93940	ATTN: LKD R. Narcisi (1 cy)
ATTN: CODE 1424 Lib	ATTN: LKO R. Van Tassel (1 cy)
ATTN: CODE 61 MN E. Milne	ATTN: OPR A. Rahbee (1 cy)
	ATTN: CA A. T. Stair (1 cy)
Commanding Officer	ATTN: OPR H. Gardiner (1 cy)
Naval Research Laboratory	ATTN: OPR R. O'Neil (1 cy)
Washington, DC 20375	ATTN: OPR R. Murphy (1 cy)
ATTN: CODE 7550 J. Davis	ATTN: OPR R. Sharma (1 cy)
ATTN: CODE 4780 S. Ossakow	ATTN: PHI J. Buchau (1 cy)
ATTN: CODE 7122 D. McNutt	ATTN: XOP F. DelGreco (1 cy)
ATTN: CODE 2627 (Tech Lib)	ATTN: PHP (1 cy)
Office of Naval Research	ATTN: OPR W. Blumberg (1 cy)
Arlington, VA 22217	ATTN: LKB D. Katayama (1 cy)
ATTN: CODE 464 G. Joiner	
ATTN: CODE 421 B. Junker	

Chief US Army Research Office P. O. Box 12211 Triangle Park, NC 27709 ATTN: R. Mace ATTN: D. Squires	(1 cy)	Department of Energy Argonne National Laboratory 9700 South Cass Ave. Argonne, IL 60439 ATTN: D. Green ATTN: S. Gabelnick ATTN: G. Reedy	(1 cy) (1 cy) (1 cy)
Air Force Office of Scientific Rsch Bolling AFB, DC 20332 ATTN: Tech Lib ATTN: D. Ball ATTN: R. Kelley ATTN: T. Cress ATTN: W. Thorpe	(1 cy) (1 cy) (1 cy) (1 cy) (1 cy)	Aerodyne Research, Inc. Bedford Research Park Crosby Drive Bedford, MA 01730 ATTN: C. Kolb	(1 cy)
Air Force Weapons Laboratory, AFSC Kirtland AFB, NM 87117 ATTN: CA A. Guenther ATTN: ALPS S. Davis	(1 cy) (1 cy)	Aerospace Corp. P. O. Box 92957 Los Angeles, CA 90009 ATTN: N. Cohen ATTN: L. Weeks ATTN: R. Herm	(1 cy) (1 cy) (1 cy)
Director Air University Library Department of the Air Force Maxwell AFB, AL 36112 ATTN: AUL-LSE	(1 cy)	AVCO Everett Research Lab, Inc. 2385 Revere Beach Parkway Everett, MA 02149 ATTN: Tech Library ATTN: C. Von Rosenberg Jr.	(1 cy) (1 cy)
Department of Commerce National Bureau of Standards 325 Broadway Boulder, CO 80302 ATTN: A. Phelps ATTN: S. Leone	(1 cy) (1 cy)	National Science Foundation 1800 G Street, NW Washington, DC 20556 ATTN: R. Sinclair ATTN: Div of Atmos Sci ATTN: W.C. Cramer	(1 cy) (1 cy) (1 cy)
Department of Commerce National Oceanic & Atmospheric Admin Environmental Research Laboratories Boulder, CO 80302 ATTN: F. Fehsenfeld ATTN: E. Ferguson	(1 cy) (1 cy)	Boston College Space Data Analysis Lab 885 Centre Street Newton, MA 02159 ATTN: W. Grieder ATTN: E. Hegblom	(1 cy) (1 cy)
Director F. J. Seiler Research Laboratory USAF Academy, CO	(1 cy)	California Institute of Technology Arthur D. Doyes Laboratory of Chem Physics Pasadena, CA 91125 ATTN: J. Beauchamp	(1 cy)
AFIT/ENP Wright-Patterson AFB, OH 45433 ATTN: E. Dorko	(1 cy)	Concord Sciences P. O. Box 119 Concord, MA 01742 ATTN: E. Sutton	(1 cy)
Department of Energy Los Alamos National Laboratory Los Alamos, NM 87545 ATTN: NSP/T&V R. Jeffreys ATTN: AP-DO W. Maier ATTN: CMB-1 R. Engleman ATTN: CMB-1 T. Bienewski ATTN: CNC-2 G. Streit ATTN: ESS-7 D. Cobb ATTN: ESS-8 M. Pongratz ATTN: ESS-7 J. Zinn ATTN: ESS-7 D. Sappenfield ATTN: T-12 D. Cartwright ATTN: ESS-5 B. Sanford	(1 cy) (1 cy)	General Electric Co. Space Division Valley Forge Space Center P. O. Box 8555 Philadelphia, PA 19101 ATTN: F. Alyea ATTN: M. Bortner ATTN: P. Zavitsanos	(1 cy) (1 cy) (1 cy)

HSS, Inc. 2 Alfred Circle Bedford, MA 01730 ATTN: M. Shuler ATTN: D. Hansen	(1 cy) (1 cy)	Science Applications, Inc. P. O. Box 1303 McLean, VA 22102 ATTN: E. Hyman	(1 cy)
Dept of Physics University of Denver Denver, CO 80208 ATTN: D. Murcray	(1 cy)	Physical Sciences, Inc. Research Park Andover, MA 01810 ATTN: G. Caledonia	(1 cy)
Toyon Research Corp. 5951 Encina Rd., Suite 229 Goleta, CA 93117 ATTN: J. Ise	(1 cy)	Pittsburgh, University of Cathedral of Learning Pittsburgh, PA 15260 ATTN: W. Fite ATTN: F. Biondi ATTN: F. Kaufman	(1 cy) (1 cy) (1 cy)
Photometrics, Inc. 4 Arrow Drive Woburn, MA 01801 ATTN: I. Kofsky	(1 cy)	R&D Associates P. O. Box 9695 Marina Del Rey, CA 90291 ATTN: F. Gilmore ATTN: R. Lelevier	(1 cy) (1 cy)
Johns Hopkins University Applied Physics Lab Johns Hopkins Road Laurel, MD 20820 ATTN: M. Linevsky	(1 cy)	SRI International 333 Ravenswood Avenue Menlo Park, CA 94025 ATTN: W. Chesnut ATTN: D. Hildenbrand	(1 cy) (1 cy)
KAMAN TEMPO 816 State Street (P.O. Drawer QQ) Santa Barbara, CA 93102 ATTN: DASLAC ATTN: W. Knapp ATTN: T. Stephens	(1 cy) (1 cy) (1 cy)	VISIDYNE, Inc. 5 Corporate Place South Bedford Street Burlington, MA 01803 ATTN: W. Reidy ATTN: C. Humphrey ATTN: T. Degges ATTN: J. Carpenter ATTN: H. Smith	(1 cy) (1 cy) (1 cy) (1 cy) (1 cy)
Lawrence Livermore National Lab P.O. Box 808 Livermore, CA 94550 ATTN: DOC CON FOR L-71 J. Chang	(1 cy)	Department of Commerce National Bureau of Standards Washington, DC 20234 ATTN: SEC OFC FOR L. Gevantman ATTN: SEC OFC FOR M. Krauss ATTN: SEC OFC FOR S. Abramowitz	(1 cy) (1 cy) (1 cy) (1 cy)
Mission Research Corp. P.O. Drawer 719 Santa Barbara, CA 93102 ATTN: M. Scheibe ATTN: D. Archer ATTN: F. Fajen ATTN: R. Kilb	(1 cy) (1 cy) (1 cy) (1 cy)	Nichols Research 4040 S. Memorial Parkway Huntsville, AL 35802 ATTN: P. Atha	(1 cy)
Stewart Radiance Laboratory Utah State University 139 Great Rd. Bedford, MA 01730 ATTN: J. Ulwick	(1 cy)		
United Technologies Research Ctr East Hartford, CT 06108 ATTN: H. Michels	(1 cy)		

END

FILMED

3-84

DTIC